








Article

ACTN2 Mutant Causes Proteopathy in Human iPSC-Derived Cardiomyocytes

Antonia T. L. Zech ^{1,2,†}, Maksymilian Prondzynski ^{1,2,3,†} , Sonia R. Singh ^{1,2}, Niels Pietsch ^{1,2}, Ellen Orthey ^{1,2}, Erda Alizoti ^{1,2}, Josefine Busch ^{1,2}, Alexandra Madsen ^{1,2}, Charlotta S. Behrens ^{1,2}, Moritz Meyer-Jens ^{1,2} , Giulia Mearini ^{1,2}, Marc D. Lemoine ^{1,2,4} , Elisabeth Krämer ^{1,2}, Diogo Mosqueira ⁵, Sanamjeet Viridi ⁶, Daniela Indenbirken ⁶, Maren Depke ⁷, Manuela Gesell Salazar ⁷ , Uwe Völker ^{7,8} , Ingke Braren ⁹, William T. Pu ^{3,10}, Thomas Eschenhagen ^{1,2}, Elke Hammer ^{7,8} , Saskia Schlossarek ^{1,2} and Lucie Carrier ^{1,2,*} 

- ¹ Institute of Experimental Pharmacology and Toxicology, University Medical Center Hamburg-Eppendorf, 20246 Hamburg, Germany
 - ² DZHK (German Centre for Cardiovascular Research), Partner Site Hamburg/Kiel/Lübeck, 20246 Hamburg, Germany
 - ³ Department of Cardiology, Boston Children's Hospital, Harvard Medical School, Boston, MA 02115, USA
 - ⁴ Department of Cardiology, University Heart and Vascular Center, 20246 Hamburg, Germany
 - ⁵ Biodiscovery Institute, University of Nottingham, Nottingham NG7 2RD, UK
 - ⁶ Heinrich-Pette-Institute, Leibniz Institute of Virology, 20246 Hamburg, Germany
 - ⁷ Department for Functional Genomics, Interfaculty Institute for Genetics and Functional Genomics, University Medicine Greifswald, 17475 Greifswald, Germany
 - ⁸ DZHK (German Centre for Cardiovascular Research), Partner Site Greifswald, 17475 Greifswald, Germany
 - ⁹ Vector Facility, University Medical Center Hamburg-Eppendorf, 20246 Hamburg, Germany
 - ¹⁰ Harvard Stem Cell Institute, Cambridge, MA 02138, USA
- * Correspondence: l.carrier@uke.de; Tel.: +49-40-7410-57208
† These authors contributed equally to this work.



Citation: Zech, A.T.L.; Prondzynski, M.; Singh, S.R.; Pietsch, N.; Orthey, E.; Alizoti, E.; Busch, J.; Madsen, A.; Behrens, C.S.; Meyer-Jens, M.; et al. ACTN2 Mutant Causes Proteopathy in Human iPSC-Derived Cardiomyocytes. *Cells* **2022**, *11*, 2745. <https://doi.org/10.3390/cells11172745>

Academic Editor: Agapios Sachinidis

Received: 9 August 2022

Accepted: 29 August 2022

Published: 2 September 2022

Publisher's Note: MDPI stays neutral with regard to jurisdictional claims in published maps and institutional affiliations.



Copyright: © 2022 by the authors. Licensee MDPI, Basel, Switzerland. This article is an open access article distributed under the terms and conditions of the Creative Commons Attribution (CC BY) license (<https://creativecommons.org/licenses/by/4.0/>).

Abstract: Genetic variants in α -actinin-2 (ACTN2) are associated with several forms of (cardio)myopathy. We previously reported a heterozygous missense (c.740C>T) ACTN2 gene variant, associated with hypertrophic cardiomyopathy, and characterized by an electro-mechanical phenotype in human induced pluripotent stem cell-derived cardiomyocytes (hiPSC-CMs). Here, we created with CRISPR/Cas9 genetic tools two heterozygous functional knock-out hiPSC lines with a second wild-type (ACTN2wt) and missense ACTN2 (ACTN2mut) allele, respectively. We evaluated their impact on cardiomyocyte structure and function, using a combination of different technologies, including immunofluorescence and live cell imaging, RNA-seq, and mass spectrometry. This study showed that ACTN2mut presents a higher percentage of multinucleation, protein aggregation, hypertrophy, myofibrillar disarray, and activation of both the ubiquitin-proteasome system and the autophagy-lysosomal pathway as compared to ACTN2wt in 2D-cultured hiPSC-CMs. Furthermore, the expression of ACTN2mut was associated with a marked reduction of sarcomere-associated protein levels in 2D-cultured hiPSC-CMs and force impairment in engineered heart tissues. In conclusion, our study highlights the activation of proteolytic systems in ACTN2mut hiPSC-CMs likely to cope with ACTN2 aggregation and therefore directs towards proteopathy as an additional cellular pathology caused by this ACTN2 variant, which may contribute to human ACTN2-associated cardiomyopathies.

Keywords: α -actinin-2; protein aggregation; ubiquitin-proteasome system; autophagy; sarcomere; inherited cardiomyopathy; human induced pluripotent stem cell-derived cardiomyocytes

1. Introduction

α -actinin-2 (ACTN2) is a component of the sarcomere in skeletal and cardiac myocytes, which forms anti-parallel homodimers that can anchor and crosslink actin thin filaments to the Z-disk (for reviews, see [1,2]). Additionally, ACTN2 is implicated in assembling large

protein complexes for structural integrity, mechanotransduction, and cell signaling (for reviews, see [3,4]).

Genetic variants in *ACTN2* are associated in the heterozygous state with common inherited cardiac diseases, which are hypertrophic (HCM), dilated (DCM), and restrictive (RCM) cardiomyopathy [5–8]. Although considered a rare disease gene [9], recent reports showed the association of homozygous *ACTN2* variants with core myopathy [10], or progressive, severe RCM [6]. In addition, it was shown that heterozygous *ACTN2* variants have critical effects on the structure and function of the cardiac muscle [11]. We previously demonstrated that a heterozygous HCM missense *ACTN2* variant (c.740C>T) induced an electro-mechanical phenotype in human-induced pluripotent stem cell-derived cardiomyocytes (hiPSC-CMs; [8]). The molecular mechanisms by which missense *ACTN2* variants lead to different forms of (cardio)myopathy are not fully understood. It is assumed that mutant transcripts are translated into proteins, which are expected to have a dominant-negative effect on sarcomere structure and/or function. However, mutant proteins can also be misfolded and targeted toward the ubiquitin-proteasome system (UPS) for degradation or can form aggregates, causing cellular proteopathy if not targeted for degradation toward the autophagy-lysosomal pathway (ALP; [12–14]).

In this study, we created with CRISPR/Cas9 genetic tools two cell lines expressing either a wild-type *ACTN2* (*ACTN2*_{wt}; c.740C) or a mutant *ACTN2* (*ACTN2*_{mut}; c.740T) and evaluated the impact of the mutant *ACTN2* on cellular structure and function in hiPSC-CMs, using a combination of different technologies, including immunofluorescence and live cell imaging, RNA-seq, and mass spectrometry (MS) analyses. Our data showed that the *ACTN2*_{mut} hiPSC-CMs present hypertrophy, myofibrillar disarray, *ACTN2* aggregation, a higher percentage of multinucleation, and activation of both UPS and ALP. It was associated with a marked reduction of sarcomere-associated protein levels and force impairment in engineered heart tissues (EHTs). Our data indicate proteopathy as an additional cellular feature caused by the missense *ACTN2* variant, which may contribute to human *ACTN2*-associated cardiomyopathy.

2. Materials and Methods

2.1. Generation and Culture of hiPSC-CMs in 2D and EHT Formats

Cultivation, CRISPR/Cas9 gene editing, and differentiation of hiPSC lines into CMs were performed as described previously [8]. A detailed methodology is provided in the Supplementary Materials.

2.2. Morphological Analysis of 2D-Cultured hiPSC-CMs

Quantification of myofibrillar disarray and cell area was evaluated with Fiji (ImageJ) as described previously [8,15]. Detailed information for *ACTN2* protein aggregate analysis and hiPSC-CMs volume measurement is provided in the Supplementary Materials.

2.3. Production and Purification of Adeno-Associated Virus Vector Particles

The production and purification of adeno-associated virus serotype 6 (AAV6) vector particles carrying the mTagRFP-mWasabi-hLC3 tandem construct, and the WT- or MUT-*ACTN2*-HaloTag[®] was adapted from a recent publication [16]. A detailed protocol is provided in the Supplementary Materials.

2.4. Proteome Analysis

Sample preparation (n = pool of 2–3 replicates per batch from 3 independent differentiation batches), protein digestion, and liquid chromatography–tandem MS were performed as described previously [17,18]. Detailed information is provided in the Supplementary Materials (Tables S4–S6).

2.5. High-Content Imaging of Autophagy-Lysosomal Pathway in hiPSC-CMs

A high-content screen for ALP activity was performed in 2D-cultured hiPSC-CMs transduced with an AAV6 encoding the mTagRFP-mWasabi-hLC3 tandem construct under the control of a human *TNNT2* promoter. After 30 days of culture, hiPSC-CMs were fixed, stained with a cardiac troponin T antibody (TNNT2, 1:500; ab45932) and with Hoechst 33342 for nuclei staining (1 µg/mL; Thermo Fisher Scientific, Waltham, MA, USA), and imaged with the Operetta high-content imaging system (PerkinElmer, Nottingham, UK). Subsequent image analysis was performed with the Harmony high-content imaging analysis software (PerkinElmer, Nottingham, UK) by identifying TNNT2+ cells and quantifying green and red puncta (number and intensity). A detailed method is described in the Supplementary Materials.

2.6. Statistics

Group data are presented as mean ± SEM. GraphPad Prism 9 (GraphPad Software, San Diego, CA, USA) was used for data analysis. Curves were fitted to data points from individual experiments. When two groups were analyzed, data were compared with the unpaired Student's *t*-test, nested *t*-tests when appropriate, or two-way ANOVA followed by Tukey's post-test, as described in the figure legends. Chi-square analysis was performed for multinucleation and integration/aggregation analysis, whereby each data set was compared to ACTN2wt using "compare observed distribution with expected" and the Wilson/Brown method. A mixed-effects analysis plus Sidak's post-test was performed when pooled batches of two cell lines were analyzed over a timeline. A *p*-value < 0.05 was considered statistically significant.

3. Results

3.1. ACTN2mut 2D-Cultured hiPSC-CMs Display Hypertrophy, Myofibrillar Disarray, Protein Aggregation, and Multinucleation

Both ACTN2wt and ACTN2mut lines were derived from the previously described heterozygous ACTN2 HCM hiPSC line (ACTN2het; c.740C>T; [8]) using CRISPR/Cas9 gene editing and homology-directed repair. Initially, both hiPSC lines were intended to produce an isogenic control without the mutation. However, sequencing analysis revealed only one functional wild-type allele in ACTN2wt [19] and only one functional mutant allele in ACTN2mut (Figure S1A). The other allele of both cell lines contained on-target defects of CRISPR/Cas9 (splice-site mutation in ACTN2wt [19] and large rearrangement in ACTN2mut (Figure S1A,B)), leading to nonsense mRNAs, which are not visible by RNA-seq (Figure S2D). Thus, we created two heterozygous functional knock-out lines with a second wild-type and missense ACTN2 allele, respectively. Both ACTN2wt and ACTN2mut hiPSC lines presented a normal karyotype (Figure S1C) and were therefore differentiated to hiPSC-CMs according to our protocol (Figure S1D). HiPSC-CMs were produced with high purity (on average >90% cardiac troponin T (TNNT2)-positive cells) and quantity (Figure S2A).

Both hiPSC-CM lines were evaluated for ACTN2 abundance and localization, myofibrillar disarray, cellular hypertrophy and multinucleation. Immunofluorescence analysis revealed a cross-striated pattern of TNNT2 in both hiPSC-CM lines, indicating the proper formation of sarcomeres (Figure 1A). However, ACTN2 was less organized and formed aggregates in ACTN2mut when compared to ACTN2wt hiPSC-CMs. Quantification revealed a higher index of myofibrillar disarray and more ACTN2 aggregates in ACTN2mut hiPSC-CMs (Figure 1B,C). Further, cell area and volume were higher in ACTN2mut hiPSC-CMs (Figure 1D,E). Finally, the percentage of multinucleated (>1 nucleus) hiPSC-CMs was higher in ACTN2mut than in ACTN2wt (Figure 1F). The mononucleated-to-multinucleated ratio was 80:20 in ACTN2wt hiPSC-CMs, supporting the previous estimation obtained in human hearts [20], whereas it was 53:47 in ACTN2mut, as reported in other HCM hiPSC-CMs [21]. ACTN2 mRNA level did not differ between the two hiPSC-CM lines

(Figure S2C,E), whereas ACTN2 protein level was markedly lower in ACTN2mut hiPSC-CMs (Figure S2F,G).

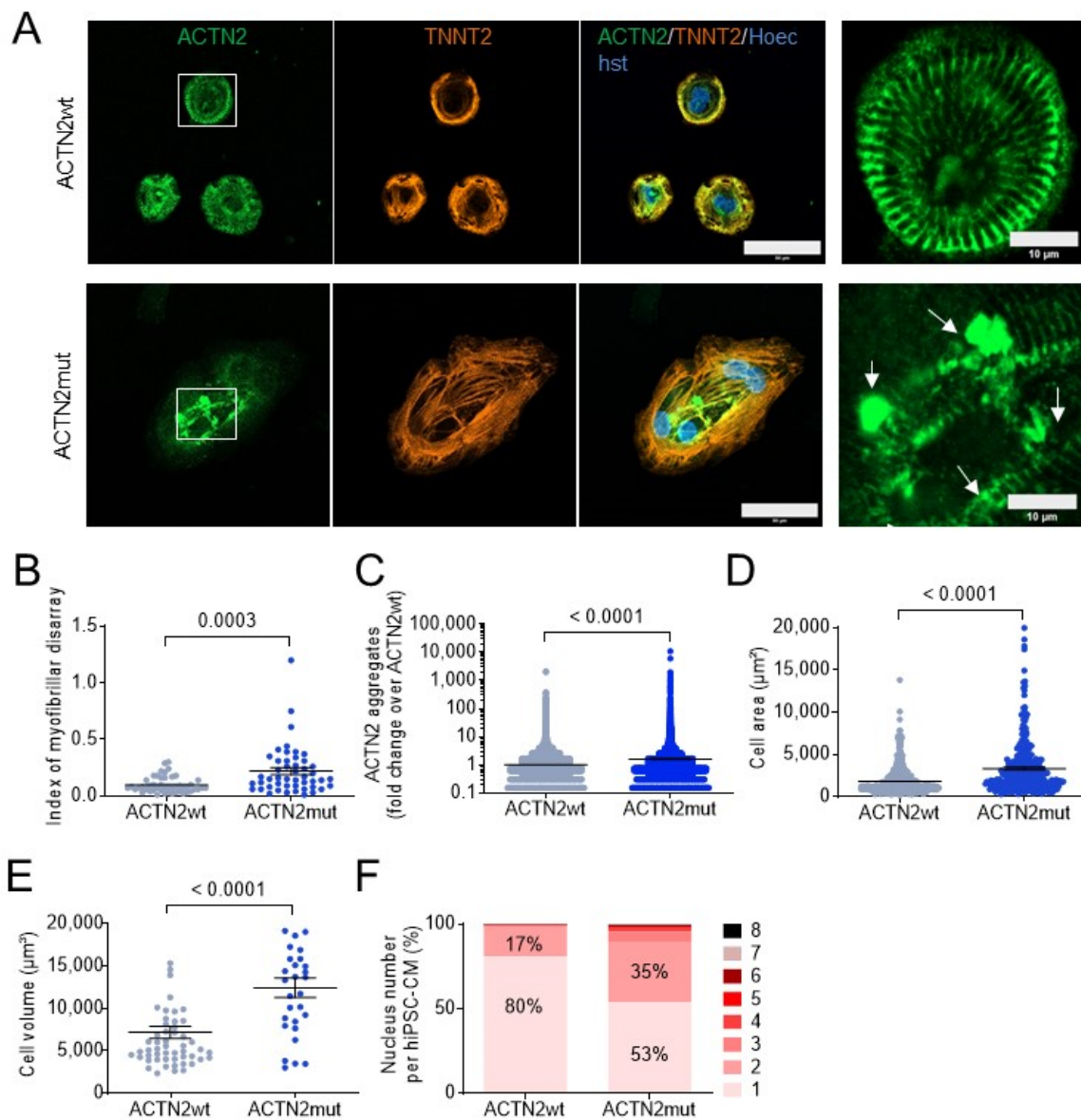


Figure 1. Disease modeling in 30-day-old, 2D-cultured hiPSC-CMs. (A) Representative immunofluorescence images of hiPSC-CMs (scale bar = 50 μm), including a higher magnification on the right (scale bar = 10 μm). After 30 days, hiPSC-CMs were fixed and stained with antibodies against ACTN2 and TNNT2, and with Hoechst for nuclei. (B) Blinded analysis of myofibrillar disarray using high-resolution pictures (ACTN2wt and ACTN2mut: N/d = 16/3). (C) Quantification of ACTN2 aggregates analyzed with Fiji software (ACTN2wt: N/d = 14/3, ACTN2mut: N/d = 15/3). (D) Quantification of cell area was analyzed with Fiji software (ACTN2wt: N/n/d = 548/3/3, ACTN2mut: N/n/d = 319/3/3). (E) Quantification of cell volume analyzed with Imaris software (ACTN2wt: N/n/d = 54/3/3, ACTN2mut: N/n/d = 29/3/3). (F) Quantification of nucleus number per hiPSC-CM analyzed with Fiji software and expressed as percentage (ACTN2wt: N/n/d = 548/3/3, ACTN2mut: N/n/d = 319/3/3; Chi-square = 280.1, $p < 0.0001$). Data are expressed as mean \pm SEM (panels B–E) or percentages (panel F), with p -values obtained with the unpaired Student's t -test (panels B–E) or two-tailed Chi-square test (panel F). Abbreviations: TNNT2, cardiac troponin T; N/n/d, number of cells/wells/differentiations. Arrows point to aggregates.

3.2. Exogenous Mutant ACTN2 Causes Aggregate Formation Leading to Sarcomere Disarray

We then tested whether exogenous mutant ACTN2 could induce protein aggregation in living, 2D-cultured ACTN2wt hiPSC-CMs. Therefore, ACTN2wt hiPSC-CMs were transduced with AAV6 carrying the MUT-ACTN2-HaloTag[®] (c.740T) and were compared to ACTN2mut hiPSC-CMs transduced with AAV6 carrying the WT-ACTN2-HaloTag[®] (c.740C). After 7 days of culture in 96-well plates, live-cell imaging experiments were performed by staining ACTN2-HaloTag protein using TMR-ligand in combination with Hoechst (Figure 2A; and examples in Videos S1 and S2). Exogenous MUT-ACTN2 in ACTN2wt and WT-ACTN2 in ACTN2mut reversed the phenotypes, inducing aggregation in about 83% and 17% of hiPSC-CMs, respectively (Figure 2A,B). This indicates that MUT-ACTN2 causes aggregation in ACTN2wt and WT-ACTN2 reverses aggregation in ACTN2mut. Quantification of acquired live cell images for ACTN2 aggregates revealed more and larger aggregates in MUT-ACTN2-transduced ACTN2wt than in WT-ACTN2-transduced ACTN2mut (Figure 2C). Western blot analysis revealed only the endogenous ACTN2 in MUT-ACTN2-transduced ACTN2wt (Figure 2D,E), suggesting a very low level of correctly folded MUT-ACTN2, which should be visible as a larger molecular weight protein. Conversely, both exogenous and endogenous ACTN2 were detected in WT-ACTN2-transduced ACTN2mut hiPSC-CMs, with about 46% of replacement of endogenous by exogenous ACTN2 (Figure 2F,G).

Immunofluorescence analysis of hiPSC-CMs transduced with WT- or MUT-ACTN2 using antibodies directed against the HaloTag[®] and total ACTN2 revealed co-localization of WT-ACTN2-HaloTag[®] and total ACTN2 staining in ACTN2mut, confirming Z-disk integration of exogenous WT-ACTN2, whereas exogenous MUT-ACTN2 was barely detectable in ACTN2wt and exhibited co-localization with total ACTN2 in some parts (Figure 2H).

3.3. ACTN2mut hiPSC-CMs Exhibit Alterations of Several Canonical Pathways

To understand the molecular changes caused by the ACTN2 mutation, MS was performed in 2D-cultured hiPSC-CMs. Three replicates of each hiPSC-CM line were pooled, and three batches of differentiation were analyzed. Volcano plots depict 481 (250 higher, 231 lower) dysregulated proteins in ACTN2mut vs. ACTN2wt (Figure 3A). Ingenuity Pathway Analysis (IPA) revealed dysregulation of several canonical pathways, diseases, and biological functions in ACTN2mut hiPSC-CMs (Figure 3B; Dataset S1). Specifically, mitochondrial function, sirtuin signaling, protein ubiquitination, hereditary myopathy, sliding of myofilaments, and stabilization of mRNA were highly dysregulated in ACTN2mut. A deeper analysis of proteomic data revealed that the protein levels of ACTN2, several other sarcomere-associated proteins and desmosomal proteins were markedly lower in ACTN2mut hiPSC-CMs (Table S1). Some of these proteins (FLNC, MYOZ2, NEBL, SYNPO2, SYNPO2L, TTN) are known to interact directly with ACTN2 [22–24]. On the other hand, FHL1 and FHL2, located at the Z-disk of the sarcomere [25,26] were more abundant in ACTN2mut. Several proteins associated with the UPS and/or ALP (e.g., BAG3, CTSC, GBA, HSPA1A, PSMA3, PSMA6, PSMB5, PSME2, TRIM54, UBA1, UBE2O, UBQLN2) were more abundant in ACTN2mut hiPSC-CMs (Table S2).

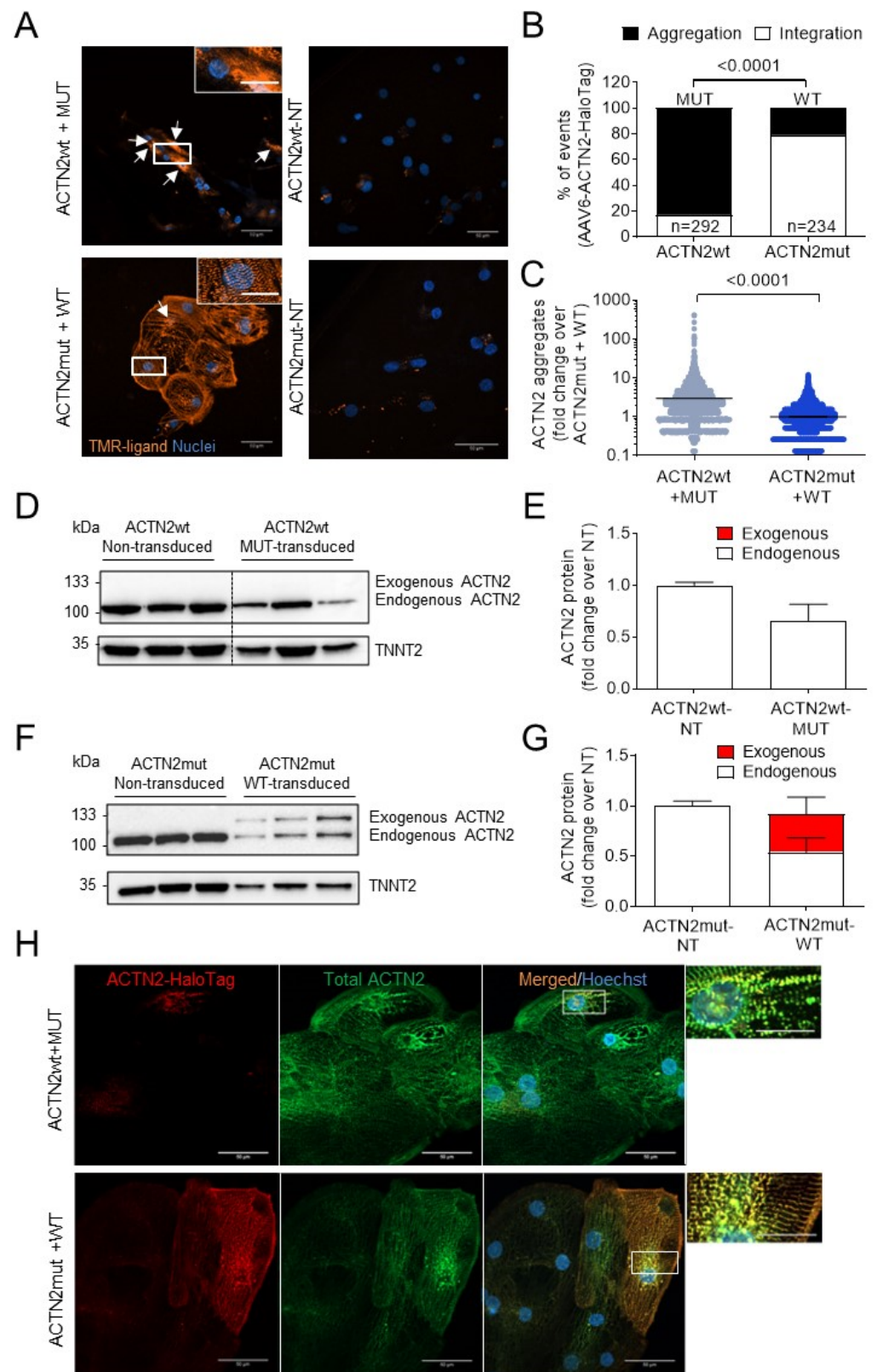


Figure 2. Live cell imaging and immunofluorescence in 2D-cultured hiPSC-CMs after 7 or 30 days in culture. (A) Representative images of ACTN2wt and ACTN2mut hiPSC-CMs transduced with an

AAV6 carrying either the *ACTN2*-MUT-HaloTag[®] or *ACTN2*-WT-HaloTag[®] construct and seeded in 96-well plates (2500–5000 cells/well). After 7 days, live cell imaging was performed by adding TMR-ligand to stain *ACTN2*-HaloTag[®] protein and Hoechst for nuclei staining (Scale bars = 50 μ m; zoom = 20 μ m). (B) Blinded quantification of sarcomere integration or aggregation of exogenous MUT-*ACTN2* in *ACTN2*wt hiPSC-CMs (N/n/d = 292/3/1) or WT-*ACTN2* in *ACTN2*mut hiPSC-CMs (N/n/d = 234/3/1). (C) Quantification of *ACTN2* aggregates in hiPSC-CM lines. Analysis was performed with Fiji software (*ACTN2*wt+MUT-*ACTN2*: N/d = 26/1, *ACTN2*mut+WT-*ACTN2*: N/d = 9/1). (D,E) Western blot stained for *ACTN2* and TNNT2 and quantification of non-transduced (NT) *ACTN2*wt or *ACTN2*wt transduced with *ACTN2*-MUT-HaloTag[®] (n/d = 3/1) after 30 days. (F,G) Western blot stained for *ACTN2* and TNNT2 and quantification of non-transduced (NT) *ACTN2*mut or *ACTN2*mut transduced with *ACTN2*-WT-HaloTag[®] (n/d = 3/1) after 30 days. (H) Representative images of fixed *ACTN2*wt and *ACTN2*mut hiPSC-CMs transduced with an AAV6 carrying either the *ACTN2*-MUT-HaloTag[®] or the *ACTN2*-WT-HaloTag[®] after 30 days of culture and stained with antibodies directed against the HaloTag[®] and *ACTN2*, and Hoechst for nuclei staining (scale bar = 50 μ m). Images were taken with a Zeiss LSM 800 microscope. Data are expressed as percentages (panel B) or as mean \pm SEM (panels C,E,G), with *p*-values obtained with one-tailed Chi-square test (panel B) or unpaired Student's *t*-test (panel C). Abbreviations: AAV6, adeno-associated virus serotype 6; MUT, mutant; NT, non-transduced; TNNT2, cardiac troponin T; WT, wild-type; N/n/d, number of cells/wells/differentiations. Arrows point to aggregates.

We then performed RNA-seq on 3 pooled replicates of each hiPSC-CM line from 3 cardiac differentiation batches. The Volcano plot showed 344 (164 higher, 180 lower) dysregulated mRNAs in *ACTN2*mut vs. *ACTN2*wt (Figure 3C). IPA analysis revealed several different dysregulated canonical pathways, diseases, and biological functions in *ACTN2*mut when compared to *ACTN2*wt (Figure 3D; Dataset S2). Some of the highlighted IPA pathways were metabolism, hypoxia, oxidative and cellular stress, cardiac hypertrophy, and cellular remodeling, whereas signaling of actin cytoskeleton was less pronounced. Specifically, the mRNA levels of sarcomere-associated proteins did not differ between the two groups, except for *FHL2* and *MYH6*, which were lower and higher in *ACTN2*mut than in *ACTN2*wt, respectively (Table S1). These data were confirmed by mRNA count analysis using the nanoString nCounter[®] Elements technology (Figure S2E). RNA-seq also revealed dysregulation of several genes, encoding proteins involved in the UPS and ALP in *ACTN2*mut hiPSC-CMs (Table S2).

Taken together, Omics analysis supported experimental findings for structural sarcomere abnormalities in *ACTN2*mut hiPSC-CMs and suggested alterations in pathways such as cellular stress response, cell survival/apoptosis or protein homeostasis, which directly point towards proteopathy as an important disease feature.

3.4. *ACTN2*mut hiPSC-CMs Exhibit Higher Activities of the Ubiquitin-Proteasome System and the Autophagy-Lysosomal Pathway

The higher abundance of several UPS- and/or ALP-associated proteins and the presence of *ACTN2* aggregates in *ACTN2*mut hiPSC-CMs suggested an altered proteostasis. Therefore, the activity of both systems was evaluated in 2D-cultured hiPSC-CMs. To evaluate the UPS, cells were treated either with vehicle (0.05% DMSO) or the UPS inhibitor epoxomicin (250 nM; Figure 4A–D). Under basal conditions (DMSO), the levels of (poly)ubiquitinated proteins and of their shuttle protein for autophagy-mediated degradation SQSTM1 did not differ between cell lines, whereas *ACTN2* level was lower in *ACTN2*mut than *ACTN2*wt, reproducing our findings (Figure S2F,G). Epoxomicin treatment induced a marked accumulation of (poly)ubiquitinated proteins and SQSTM1 in both hiPSC-CMs (Figure 4A–C), validating the efficacy of the treatment. In contrast, epoxomicin did not increase the level of *ACTN2* in any cell line, indicating that *ACTN2* was not degraded by the UPS in this experimental condition (Figure 4A,D). On the other hand, the chymotrypsin-like activity of the proteasome was markedly higher in *ACTN2*mut hiPSC-CMs (Figure 4E), suggesting UPS activation.

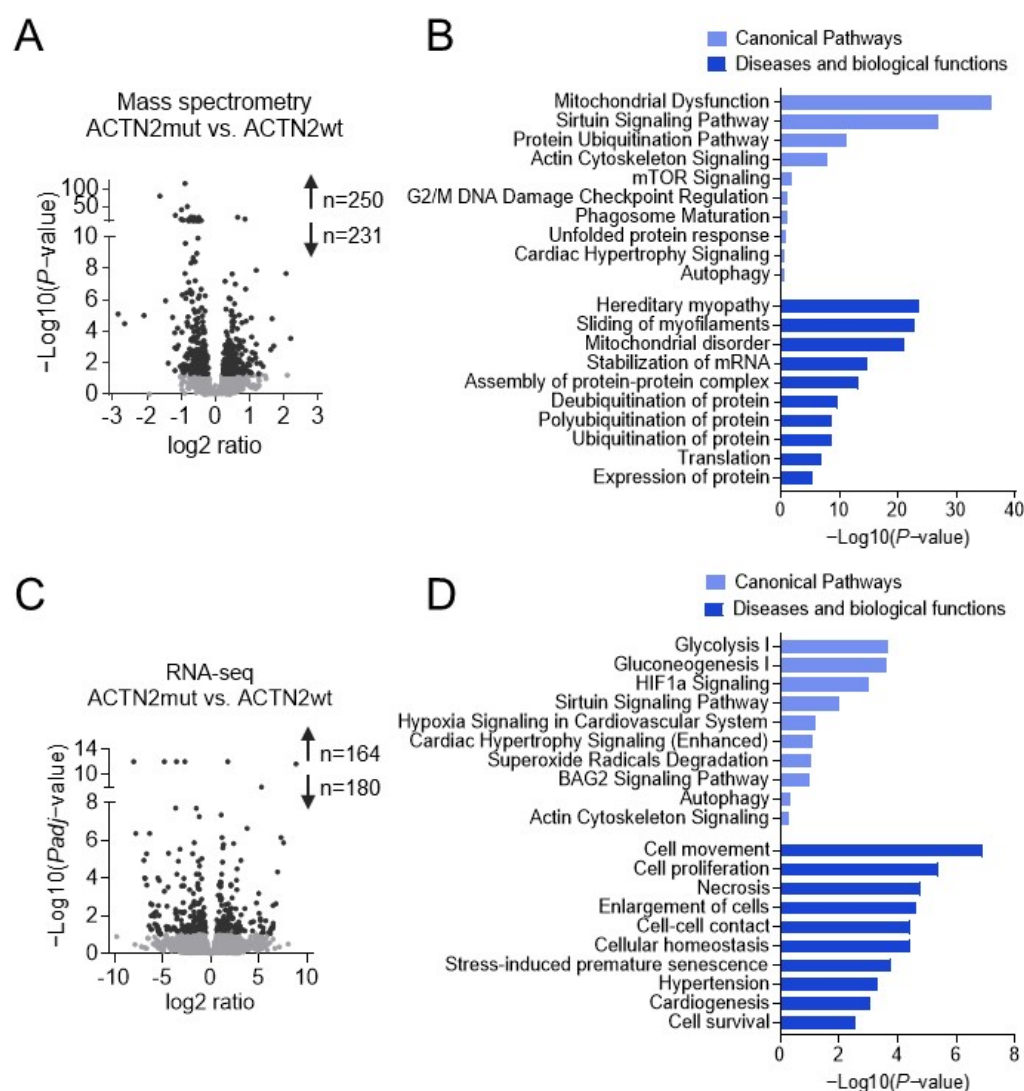


Figure 3. MS and RNA-seq analysis of 30-day-old, 2D-cultured hiPSC-CMs. **(A)** Alterations in protein levels between ACTN2mut vs. ACTN2wt (250 up, 231 down) hiPSC-CMs based on MS are displayed in a volcano plot that shows the $-\text{Log}_{10}$ of p -value vs. magnitude of change (\log_2 ratio) whereby light grey dots indicate $p > 0.05$ and dark grey dots $p < 0.05$. **(B)** Selected hits of significantly dysregulated canonical pathways and biological functions in 2D-cultured ACTN2mut vs. ACTN2wt hiPSC-CMs based on MS analysis using Ingenuity Pathway Analysis (IPA). Unsupervised IPA was performed for significantly altered proteins (Fisher's exact test; $p < 0.05$). **(C)** Alterations in mRNA levels in ACTN2mut vs. ACTN2wt (164 up, 180 down) hiPSC-CMs based on RNA-seq analysis are displayed in a volcano plot that shows the $-\text{Log}_{10}$ of P_{adj} -value vs. magnitude of change (\log_2 ratio) whereby light grey dots indicate $FDR > 0.1$ and dark grey dots $FDR < 0.1$. **(D)** Selected hits of significantly dysregulated canonical pathways and biological functions in 2D-cultured ACTN2mut vs. ACTN2wt hiPSC-CMs based on RNA-seq analysis using IPA. Unsupervised IPA was performed for significantly altered genes (Fisher's exact test; $FDR < 0.1$).

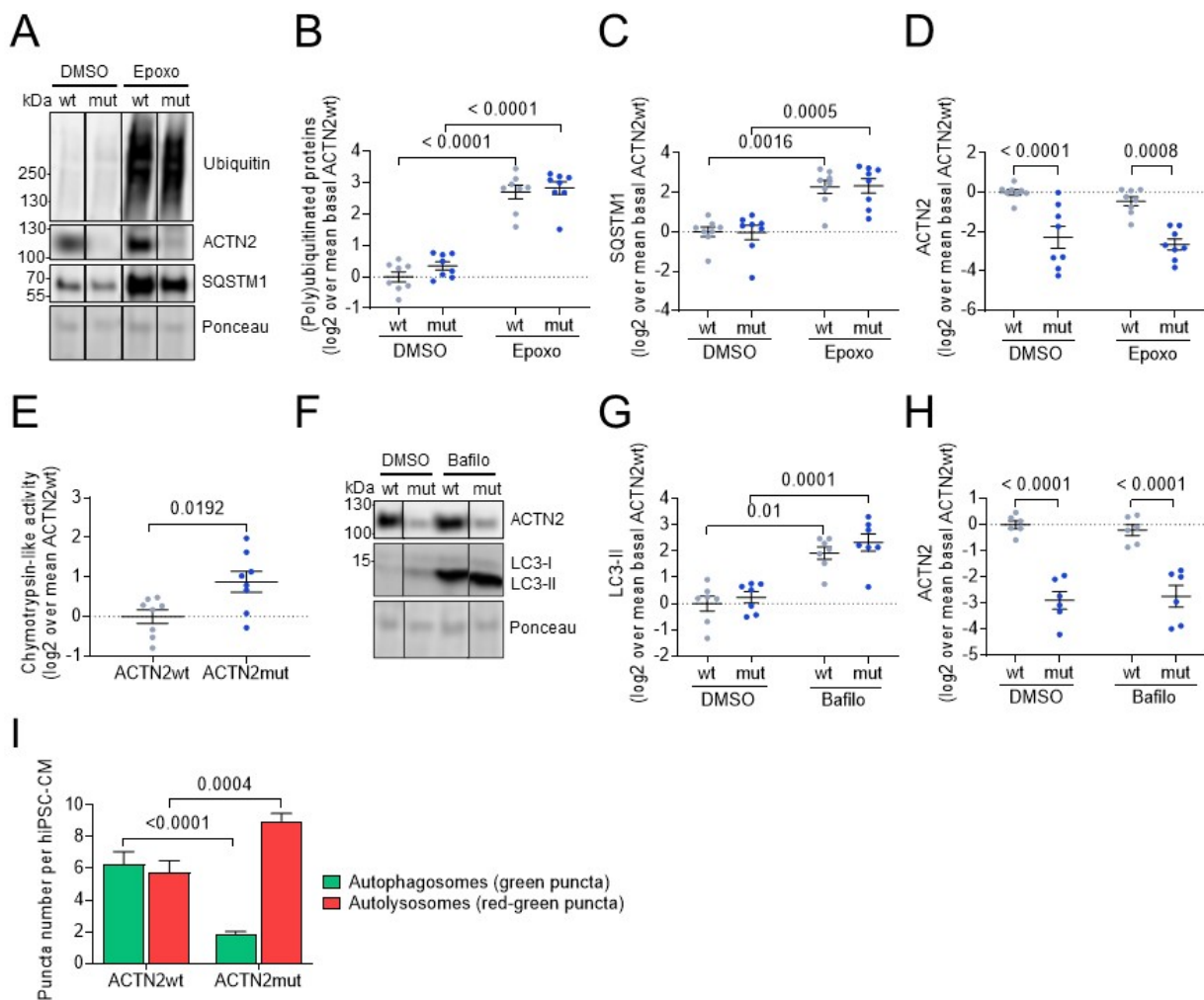


Figure 4. Evaluation of the impact of the *ACTN2* gene variant on the proteolytic systems in 30-day-old, 2D-cultured hiPSC-CMs. Representative Western blots and Ponceau (**A**), and quantification, normalized to Ponceau, of the levels of (**B**) (poly)ubiquitinated proteins, (**C**) SQSTM1, (**D**) ACTN2 in hiPSC-CMs treated with DMSO (0.05%) or epoxomicin (Epoxo; 250 nM) for 16.5 h at 37 °C (ACTN2wt: n/d = 7–8/3, ACTN2mut: n/d = 7–8/3). (**E**) Chymotrypsin-like activity of the proteasome in hiPSC-CMs (ACTN2wt: n/d = 8/3, ACTN2mut: n/d = 8/3). (**F**) Representative Western blots, Ponceau, and quantification of protein levels of (**G**) LC3-II and (**H**) ACTN2 of hiPSC-CMs treated with DMSO (0.05%) or bafilomycin A1 (Bafilo; 50 nM) for 3 h at 37 °C (ACTN2wt: n/d = 6–7/3, ACTN2mut: n/d = 6–7/3). (**I**) The ALP activity was indirectly measured by determining the number of autophagosomes (green puncta) and autolysosomes (red minus green puncta) whereby the number of puncta is related to the CM number per well (ACTN2wt and ACTN2mut: n = 9). Data are expressed as mean ± SEM, with *p*-values obtained with two-way ANOVA and Tukey’s post-test (panels **B–D**, **G–I**) or with unpaired Student’s *t*-test (panels **E**). Abbreviations: n/d, number of wells/differentiations.

To evaluate the ALP, the autophagic flux was measured in hiPSC-CMs after treatment with either DMSO (0.05%) or the late-stage ALP inhibitor bafilomycin A1 (50 nM; Figure 4F–H). The level of microtubule-associated protein 1 light chain 3b-II (LC3-II) did not differ between the genotypes in basal conditions. Treatment with bafilomycin A1 markedly increased LC3-II levels in both groups (Figure 4F,G). The difference in LC3-II level between bafilomycin-treated and DMSO-treated samples, which represents the autophagic flux, was higher in ACTN2mut than in ACTN2wt (difference in log₂, ACTN2wt: 1.93, ACTN2mut: 2.09). On the other hand, bafilomycin A1 did not increase ACTN2

levels (Figure 4H), implying that ACTN2 is not degraded by the ALP. To support the autophagic flux data, we performed a high-content imaging in the hiPSC-CM lines transduced with an AAV6 encoding mTagRFP-mWasabi-hLC3 under the control of the *TNNT2* promoter. After 30 days of culture, hiPSC-CMs were fixed and immunostained for TNNT2 and Hoechst to ensure imaging of (solely) cardiomyocytes (Figure S3A; >80% TNNT2+, data not shown). The number of green and red puncta per well was quantified using an unbiased and statistically powerful method and normalized to the number of hiPSC-CMs per well. The number of green puncta per hiPSC-CM was markedly lower in ACTN2mut (Figure S3B), whereas the number of red puncta per hiPSC-CM did not differ between the groups (Figure S3C). The utilization of the LC3-tandem-construct allows to determine autophagosomes (AP) and autolysosomes (AL), since the green fluorescence (mWasabi) is susceptible to low pH and hence quenched within Als. Therefore, green puncta correspond to Aps, red puncta to Aps plus Als, and the difference between red and green puncta (=red minus green puncta) to Als. ACTN2wt hiPSC-CMs exhibited a similar number of Aps and Als per hiPSC-CM (Figure 4I), suggesting a steady-state autophagic flux. In contrast, the AP number per hiPSC-CM was markedly lower and the AL number per hiPSC-CM was higher in ACTN2mut (Figure 4I). The combination of low AP number and high AL number supports the view of an activation of autophagy, particularly at the step of fusion of Aps with lysosomes to form autolysosomes in ACTN2mut hiPSC-CMs.

Taken together, these data showed higher activities of both protein degradation systems in 2D-cultured ACTN2mut hiPSC-CMs, most likely to eliminate protein aggregates causing proteopathy.

3.5. ACTN2mut hiPSC-CMs Exhibit Force Impairment in Engineered Heart Tissues

The low abundance of several sarcomere-associated proteins in ACTN2mut hiPSC-CMs (Table S1) suggested an impairment of contractile function. Therefore, we assessed force amplitude and kinetics of the ACTN2wt and ACTN2mut in 3D EHTs after 30 days (Figure 5A,B). Unpaced ACTN2mut EHTs developed significantly lower force starting from day 9 onwards than ACTN2wt EHTs (Figure 5C). Beating frequency was significantly higher in ACTN2mut than in ACTN2wt EHTs (50 vs. 28 beats per minute from day 21 on, respectively) (Figure 5D). To compare functional parameters independent of variable baseline frequencies, EHTs were subjected to electrical pacing at 1 Hz (Videos S3 and S4). Contraction traces of EHTs showed markedly lower force in ACTN2mut than ACTN2wt EHTs (Figure 5E,F). Normalized averaged force exhibited 19% shorter time to peak ($TTP_{-80\%}$; Figure 5G,H) and 25% shorter relaxation time ($RT_{80\%}$; Figure 5G,I) in ACTN2mut EHTs. Similar results were obtained at 1.5 and 2 Hz (data not shown). Overall, ACTN2mut EHTs exhibited a significant force impairment, which can be explained by the marked deficiency of sarcomere-associated proteins detected in 2D-cultured hiPSC-CMs (Table S1) and EHTs (Table S3).

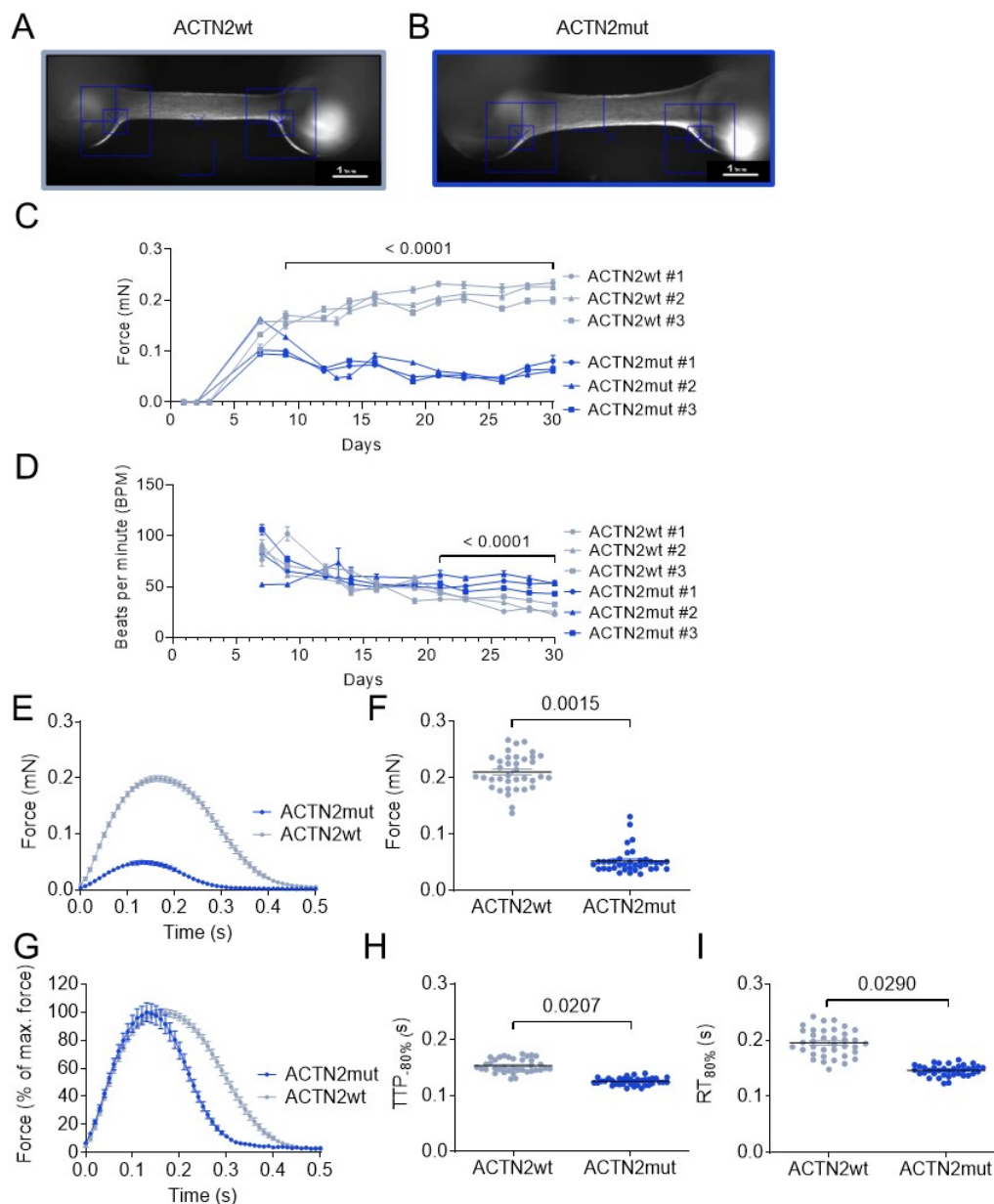


Figure 5. Force measurements in 3D-cultured hiPSC-engineered heart tissues. Representative images of (A) ACTN2wt and (B) ACTN2mut EHTs cultured for 30 days (scale bar = 1 mm). (C) Force and (D) beats per minute were measured under unpaced conditions in EHT culture medium or in 1.8 mM Ca^{2+} Tyrode's solution at 37 °C (ACTN2wt: N/d = 27–44/3, ACTN2mut: N/d = 32–44/3). (E) Average force, (F) force, (G) normalized force, (H) time to peak –80% ($\text{TTP}_{80\%}$), and (I) relaxation time to baseline 80% ($\text{RT}_{80\%}$) were measured under paced conditions at 1 Hz in 1.8 mM Ca^{2+} Tyrode's solution at 37 °C (ACTN2wt: N/d = 37/3, ACTN2mut: N/d = 37/3); data are expressed as mean \pm SEM, with *p*-values obtained with a mixed-effects analysis plus Sidak's multiple comparison tests performed on pooled batches (Panels C,D) or with the nested *t*-test vs. ACTN2wt (Panels F,H,I). Abbreviations: EHTs, engineered heart tissues; N/d, number of EHTs/differentiations.

4. Discussion

This study investigated the cellular and functional impacts of an *ACTN2* gene variant (c.740C>T; p.Thr247Met) in hiPSC-CMs. Compared to ACTN2wt, ACTN2mut hiPSC-CMs exhibited (i) cellular hypertrophy, myofibrillar disarray, multinucleation, ACTN2 protein aggregation, and activation of both the UPS and ALP in 2D culture, (ii) a marked reduction in the levels of sarcomere-associated proteins in 2D and EHTs, and (iii) force impairment

in EHTs. These findings indicate impaired sarcomerogenesis and proteopathy as typical features in ACTN2mut.

We reproduced previous findings observed in 2D-cultured heterozygous ACTN2 (ACTN2het) hiPSC-CMs [8], such as hypertrophy and myofibrillar disarray in ACTN2mut hiPSC-CMs. Furthermore, diseased cells exhibited dysregulation of pathways involved in sarcomere function and proteostasis, and ACTN2mut EHTs exhibited force impairment, resembling a DCM phenotype [27–30]. This is in line with the low abundance of several sarcomeric proteins, including ACTN2 in ACTN2mut hiPSC-CMs, leading to a poorly developed sarcomere and possibly to a more immature cardiomyocyte state. In addition, SYNPO2 and SYNPO2L, which contribute to early assembly and stabilization of the Z-disk via interaction with filamin and ACTN2 [22,27], were also less abundant, supporting disruption of the ACTN2 interactome and deficient sarcomere development in ACTN2mut hiPSC-CMs. The reduced Z-disk integration of exogenous MUT-ACTN2 in ACTN2wt by live cell imaging supports the susceptibility of mutant ACTN2 to aggregate. Conversely, exogenous WT-ACTN2 in ACTN2mut ameliorated sarcomere integration and partially replaced endogenous mutant without changing the total level of ACTN2. The inverse correlation between sarcomere incorporation and aggregation suggests that non-incorporated mutant proteins form aggregates and contribute to the low level of ACTN2 protein in ACTN2mut hiPSC-CMs. Previous analysis of the dynamic behavior of two ACTN2 missense variants (p.Ala119Thr and p.Gly111Val), which are also located in the calponin-homology domain, revealed similar phenotypes [31]. Both mutants exhibited reduced binding affinities to F-actin by biochemical assays and alterations of Z-disk localization and dynamic behavior after gene transfer of mEos2-tagged ACTN2 in adult cardiomyocytes.

The higher levels of several proteins involved in proteostasis such as the UPS and ALP in ACTN2mut hiPSC-CMs found in this study are in agreement with previous findings in HCM septal myectomies [32]. This was associated with a higher chymotrypsin-like activity of the proteasome and global activation of the ALP in ACTN2mut hiPSC-CMs. Even though others have shown that WT ACTN2 is degraded by the UPS [33], the low ACTN2 protein level detected by Western blot and proteomic analysis in the ACTN2mut line was unlikely due to degradation by the UPS or the ALP. This suggests that the global activation of both the UPS and ALP are rather compensatory, protective mechanisms against ACTN2 aggregation. The low abundance of ACTN2 and of several other sarcomeric proteins likely reflects a reduced mRNA translation and protein incorporation into myofilament to maintain the overall stoichiometry of the sarcomere [34]. This might explain the poor and reduced formation of sarcomeres in ACTN2mut hiPSC-CMs. Alteration of Z-disk protein turnover combined with subsequent activation of autophagy has been recently reported in hiPSC-CMs carrying the p.Gly1674X or p.Val1668_Gly1674del FLNC variant, resulting in haploinsufficiency and misfolded protein, respectively [35]. Similarly, FLNC protein aggregation and myofibrillar disarray were reported in cardiac muscle specimens of HCM patients carrying the p.Gly2151Ser or p.Ala1539Thr FLNC variant, and was associated with a high risk of sudden cardiac death [36]. These data emphasized the disease-causing role of proteotoxicity in FLNC-related cardiomyopathies and presumed its therapeutic potential.

Functional deficits found in ACTN2mut EHTs are in line with a recent disease modeling study that investigated the p.Arg14del variant in phospholamban (PLN; [29]). The authors showed activation of the unfolded protein response as a compensatory, protective mechanism in the setting of PLN-caused hypocontractility in hiPSC-CMs and EHTs. These findings are further supported by the evidence of PLN protein aggregates in a p.Arg14del mouse model [37]. Interestingly, PLN aggregates and altered protein homeostasis pathways were observed before the onset of functional deficits.

To date, only one study has investigated a homozygous truncating ACTN2 variant (p.Gln860Stop) associated with RCM in mutant carriers [6]. Corresponding hiPSC-CMs displayed hypertrophy, impaired contractility, and myofibrillar disarray. In contrast to our findings, the ACTN2 protein level was not reduced. However, because of the C-terminal truncation, the authors suggested loss of protein-protein interaction as the main cause for

disease development. This implies a differing mode of action for truncating and missense *ACTN2* variants, further depending on affected functional domains. Nevertheless, these findings are in line with the diminished contractile function in *ACTN2*mut EHTs, as the patient affected by the homozygous truncating *ACTN2* variant (p.Gln860Stop) developed RCM and heart failure (HF) at the age of 23 [6]. Based on the severity of cardiomyopathy phenotypes found in this study combined with the recent evidence that *ACTN2* is linked to HF [38], it can be assumed that a patient harboring the homozygous *ACTN2* missense variant would develop DCM or RCM leading to HF.

In conclusion, this study revealed an additional cellular pathology for the p.Thr247Met *ACTN2* variant, leading to proteopathy. Our data indicate the (compensatory) activation of the proteolytic machinery in *ACTN2*mut hiPSC-CMs, likely to ‘cope’ with protein aggregation.

5. Study Limitations

When working with hiPSCs, it is important to consider possible limitations of the model such as unstable genome integrity, storage of hiPSC lines, immaturity, and reproducibility when using hiPSC-CMs (for reviews, see [39–41]). To comply with best cell culture practices, we applied regular karyotyping and genotyping and established master cell banks of each hiPSC line [42]. However, both *ACTN2*wt and *ACTN2*mut hiPSC lines were generated from the *ACTN2*het hiPSC line with CRISPR/Cas9 genetic tools and homology-directed repair (HDR). We found that both hiPSC lines have a correct WT or MUT allele, and that the other recombined allele after HDR contains additional CRISPR/Cas9-mediated on-site defect, i.e., a splicing mutation for *ACTN2*wt ([19]) and a large genomic rearrangement for *ACTN2*mut (Figure S1A,B), both leading to nonsense mRNAs (Figure S2D; [19]). Thus, the consequence is the presence of only WT mRNA and protein in the *ACTN2*wt cardiomyocytes, whereas *ACTN2*mut cardiomyocytes exhibited only MUT mRNA and protein, making these two cell lines still interesting for comparison. Another limitation is that we cannot decide whether *ACTN2* aggregate formation is detrimental, contributing to disease progression, or rather beneficial, to avoid sarcomere incorporation of the mutant protein.

Supplementary Materials: The following supporting information can be downloaded at: <https://www.mdpi.com/article/10.3390/cells11172745/s1>. Figure S1: Generation of *ACTN2*wt and *ACTN2*mut cell lines; Figure S2: Validation of cardiac differentiation and mRNA and protein analysis; Figure S3: Representative data of the high-content screening performed in 2D-cultured hiPSC-CMs; Table S1: RNA-seq and mass spectrometry analyses of sarcomere-associated proteins in 2D-cultured *ACTN2*mut vs. *ACTN2*wt hiPSC-CMs; Table S2: RNA-seq and mass spectrometry analyses of the UPS and ALP in 2D-cultured *ACTN2*mut vs. *ACTN2*wt hiPSC-CMs; Table S3: RNA-seq and mass spectrometry analyses of sarcomere-associated proteins in 3D-cultured *ACTN2*mut vs. *ACTN2*wt hiPSC-CMs; Table S4: Acronyms and names of genes evaluated with the nanoString nCounter® Elements technology; Table S5: LC-MS/MS parameter (data dependent mode, spectral library); Table S6: LC-MS/MS parameter (data independent mode; quantitative data); Supplemental experimental procedures: Ethics statement, Generation and culture of hiPSC-derived cardiomyocytes (hiPSC-CMs) in 2D and EHT formats, Southern blot DNA analysis, Immunofluorescence staining of hiPSC-CMs, Morphological analysis of 2D-cultured hiPSC-CMs, Live cell imaging of 2D-cultured hiPSC-CMs, High-content imaging of 2D cultured hiPSC-CMs, RNA isolation and gene expression analysis, Western blot analysis, Measurement of chymotrypsin-like activity of the proteasome, Proteome analysis, Production and purification of adeno-associated virus vector particle; Dataset S1: MS data of 2D *ACTN2*mut hiPSC-CMs analyzed with IPA; Dataset S2: RNA-seq data of 2D *ACTN2*mut hiPSC-CMs analyzed with IPA; Video S1: Contracting *ACTN2*wt hiPSC-CMs transduced with WT-*ACTN2* HaloTag; Video S2: Contracting *ACTN2*wt hiPSC-CMs transduced with MUT-*ACTN2* HaloTag; Video S3: Contracting *ACTN2*wt EHTs. Video S4. Contracting *ACTN2*mut EHTs [8,15,17,21,43–58].

Author Contributions: Conceptualization and analysis: A.T.L.Z., M.P. and L.C.; Methodology and Investigation: CRISPR/Cas9: M.P. and N.P.; Cloning and virus production: A.T.L.Z., S.R.S. and I.B.; Cardiac differentiation: A.T.L.Z., M.P., N.P. and A.M.; cell culture, transduction, and treatments: A.T.L.Z., M.P., M.M.-J., J.B., C.S.B., A.M. and G.M.; EHT generation, maintenance, and force measurement: A.M.; Immunofluorescence and live-cell imaging: A.T.L.Z., M.P. and J.B.; Proteomics/bioinformatics: E.H., M.D., M.G.S., U.V. and M.P.; RNA isolation and gene expression analysis: M.P., M.D.L. and E.K.; RNA-seq: D.I. and S.V.; Omics analysis: A.T.L.Z., M.P., S.V. and L.C.; Western blots: S.R.S., E.O., E.A. and S.S.; High-content imaging: D.M.; Writing—Original draft: A.T.L.Z., M.P. and L.C.; Writing—Review and editing: A.T.L.Z., M.P., S.R.S., A.M., M.D.L., M.D., D.M., U.V., W.T.P., T.E., E.H., S.S. and L.C. All authors have read and agreed to the published version of the manuscript.

Funding: This work was supported fully or in part by the German Centre for Cardiovascular Research (DZHK) to M.P., M.D.L., E.H., U.V. and L.C., German Ministry of Research Education (BMBF) to M.P., M.D.L., E.H., U.V. and L.C., Deutsche Herzstiftung (F/51/17) to Sa.S., Helmut und Charlotte Kassau Stiftung to L.C., European Research Council Advanced Grant (IndivuHeart) to T.E., Research Promotion Fund of the Faculty of Medicine (Hamburg) to A.T.L.Z., M.P. and M.D.L. (“Clinician Scientist Program” and “Project funding for young scientists”), Leducq Foundation (20CVD01) to L.C., National Centre for the Replacement, Refinement, and Reduction of Animals in Research (NC3Rs: NC/S001808/1) to D.M. and Pro Exzellenzia 4.0 to S.R.S.

Institutional Review Board Statement: All procedures were in accordance with the Code of Ethics of the World Medical Association (Declaration of Helsinki). The study was reviewed and approved by the Ethical Committee of the Ärztekammer Hamburg (PV3501).

Informed Consent Statement: The HCM patient carrying the heterozygous *ACTN2* (c.740C>T; dbSNP ID: rs755492182) mutation was recruited in the outpatient HCM clinic at the University Heart and Vascular Center Hamburg and provided written informed consent for genetic analysis and the use of skin fibroblasts [8].

Data Availability Statement: Datasets, analysis and study materials will be made available on request to other researchers for purposes of reproducing the results or replicating the procedures. The full description of materials and are provided in the Supplementary Materials. All data of OMICs experiments have been made publicly available. The mass spectrometry data have been deposited to the ProteomeXchange Consortium via the PRIDE partner repository with the dataset identifier PXD034258. The RNA-seq data have been deposited to the European Nucleotide Archive (ENA) at EMBL-EBI under accession number PRJEB52889.

Acknowledgments: We would like to dedicate this paper to the memory of our dear colleague and friend Jeff Robbins (Cincinnati, OH, USA), who was the pioneer of cardiac proteotoxicity. The authors gratefully acknowledge Birgit Klampe, Sandra Laufer and Thomas Schulze (Pharmacology, Hamburg) for participating in production of hiPSC-CMs, Malte Loos for supporting in the hiPSC-CMs treatment and fixation, and the FACS and Microscopy Imaging Facility core facilities (Hamburg). We also thank Boris V. Skryabin and Timofey Rozhdestvensky (Transgenic Animal and Genetic Engineering Models (TRAM), Faculty of Medicine of the Westfalian Wilhelms-University, Münster), for the Southern blot analysis and Kerstin Kutsche (Human Genetics, Hamburg) for fruitful discussion. Additionally, we thank Anja Wiechert for support in sample preparation and Stephan Michalik for providing the in-house R pipeline for the quantitative analysis of proteomics data.

Conflicts of Interest: A.M. is now an employee and shareholder of AstraZeneca. G.M. is now an employee at DiNAQOR. T.E. and L.C. are members of DiNAQOR Scientific Advisory Board and have shares in DiNAQOR. The remaining authors declare no competing interests.

References

1. Sjoblom, B.; Salmazo, A.; Djinovic-Carugo, K. Alpha-actinin structure and regulation. *Cell. Mol. Life Sci.* **2008**, *65*, 2688–2701. [[CrossRef](#)] [[PubMed](#)]
2. Gautel, M.; Djinovic-Carugo, K. The sarcomeric cytoskeleton: From molecules to motion. *J. Exp. Biol.* **2016**, *219*, 135–145. [[CrossRef](#)] [[PubMed](#)]
3. Broderick, M.J.; Winder, S.J. Spectrin, alpha-actinin, and dystrophin. *Adv. Protein Chem.* **2005**, *70*, 203–246. [[PubMed](#)]
4. Djinovic-Carugo, K.; Gautel, M.; Ylanne, J.; Young, P. The spectrin repeat: A structural platform for cytoskeletal protein assemblies. *FEBS Lett.* **2002**, *513*, 119–123. [[CrossRef](#)]

5. Fan, L.L.; Huang, H.; Jin, J.Y.; Li, J.J.; Chen, Y.Q.; Xiang, R. Whole-Exome Sequencing Identifies a Novel Mutation (p.L320R) of Alpha-Actinin 2 in a Chinese Family with Dilated Cardiomyopathy and Ventricular Tachycardia. *Cytogenet. Genome Res.* **2019**, *157*, 148–152. [[CrossRef](#)]
6. Lindholm, M.E.; Jimenez-Morales, D.; Zhu, H.; Seo, K.; Amar, D.; Zhao, C.; Raja, A.; Madhvani, R.; Abramowitz, S.; Espenel, C.; et al. Mono- and Biallelic Protein-Truncating Variants in Alpha-Actinin 2 Cause Cardiomyopathy Through Distinct Mechanisms. *Circ. Genom. Precis. Med.* **2021**, *14*, e003419. [[CrossRef](#)]
7. Mohapatra, B.; Jimenez, S.; Lin, J.H.; Bowles, K.R.; Coveler, K.J.; Marx, J.G.; Chrisco, M.A.; Murphy, R.T.; Lurie, P.R.; Schwartz, R.J.; et al. Mutations in the muscle LIM protein and alpha-actinin-2 genes in dilated cardiomyopathy and endocardial fibroelastosis. *Mol. Genet. Metab.* **2003**, *80*, 207–215. [[CrossRef](#)]
8. Prondzynski, M.; Lemoine, M.D.; Zech, A.T.; Horvath, A.; Di Mauro, V.; Koivumaki, J.T.; Kresin, N.; Busch, J.; Krause, T.; Kramer, E.; et al. Disease modeling of a mutation in alpha-actinin 2 guides clinical therapy in hypertrophic cardiomyopathy. *EMBO Mol. Med.* **2019**, *11*, e11115. [[CrossRef](#)]
9. Walsh, R.; Thomson, K.L.; Ware, J.S.; Funke, B.H.; Woodley, J.; McGuire, K.J.; Mazzarotto, F.; Blair, E.; Seller, A.; Taylor, J.C.; et al. Reassessment of Mendelian gene pathogenicity using 7, 855 cardiomyopathy cases and 60, 706 reference samples. *Genet. Med.* **2017**, *19*, 192–203. [[CrossRef](#)]
10. Inoue, M.; Noguchi, S.; Sonehara, K.; Nakamura-Shindo, K.; Taniguchi, A.; Kajikawa, H.; Nakamura, H.; Ishikawa, K.; Ogawa, M.; Hayashi, S.; et al. A recurrent homozygous ACTN2 variant associated with core myopathy. *Acta Neuropathol.* **2021**, *142*, 785–788. [[CrossRef](#)]
11. Chiu, C.; Bagnall, R.D.; Ingles, J.; Yeates, L.; Kennerson, M.; Donald, J.A.; Jormakka, M.; Lind, J.M.; Semsarian, C. Mutations in alpha-actinin-2 cause hypertrophic cardiomyopathy: A genome-wide analysis. *J. Am. Coll. Cardiol.* **2010**, *55*, 1127–1135. [[CrossRef](#)]
12. Sandri, M.; Robbins, J. Proteotoxicity: An underappreciated pathology in cardiac disease. *J. Mol. Cell. Cardiol.* **2014**, *71*, 3–10. [[CrossRef](#)]
13. Zech, A.T.L.; Singh, S.R.; Schlossarek, S.; Carrier, L. Autophagy in cardiomyopathies. *Biochim. Biophys. Acta Mol. Cell Res.* **2020**, *1867*, 118432. [[CrossRef](#)]
14. Kocaturk, N.M.; Gozuacik, D. Crosstalk Between Mammalian Autophagy and the Ubiquitin-Proteasome System. *Front. Cell Dev. Biol.* **2018**, *6*, 128. [[CrossRef](#)]
15. Prondzynski, M.; Kramer, E.; Laufer, S.D.; Shibamiya, A.; Pless, O.; Flenner, F.; Muller, O.J.; Munch, J.; Redwood, C.; Hansen, A.; et al. Evaluation of MYBPC3 trans-Splicing and Gene Replacement as Therapeutic Options in Human iPSC-Derived Cardiomyocytes. *Mol. Ther. Nucleic Acids* **2017**, *7*, 475–486. [[CrossRef](#)]
16. Saleem, U.; Mannhardt, I.; Braren, I.; Denning, C.; Eschenhagen, T.; Hansen, A. Force and Calcium Transients Analysis in Human Engineered Heart Tissues Reveals Positive Force-Frequency Relation at Physiological Frequency. *Stem Cell Rep.* **2020**, *14*, 312–324. [[CrossRef](#)]
17. Palma Medina, L.M.; Becker, A.K.; Michalik, S.; Yedavally, H.; Raineri, E.J.M.; Hildebrandt, P.; Gesell Salazar, M.; Surmann, K.; Pfortner, H.; Mekonnen, S.A.; et al. Metabolic Cross-talk Between Human Bronchial Epithelial Cells and Internalized Staphylococcus aureus as a Driver for Infection. *Mol. Cell Proteom.* **2019**, *18*, 892–908. [[CrossRef](#)]
18. Seidl, M.D.; Stein, J.; Hamer, S.; Pluteanu, F.; Scholz, B.; Wardelmann, E.; Hüge, A.; Witten, A.; Stoll, M.; Hammer, E.; et al. Characterization of the Genetic Program Linked to the Development of Atrial Fibrillation in CREM-IbDeltaC-X Mice. *Circ. Arrhythm. Electrophysiol.* **2017**, *10*, e005075. [[CrossRef](#)]
19. Prondzynski, M.; Lemoine, M.D.; Zech, A.T.; Horvath, A.; Di Mauro, V.; Koivumaki, J.T.; Kresin, N.; Busch, J.; Krause, T.; Kramer, E.; et al. Disease modeling of a mutation in alpha-actinin 2 guides clinical therapy in hypertrophic cardiomyopathy—Addendum. *EMBO Mol. Med.* **2022**, *14*, e16423. [[CrossRef](#)]
20. Derks, W.; Bergmann, O. Polyploidy in Cardiomyocytes: Roadblock to Heart Regeneration? *Circ. Res.* **2020**, *126*, 552–565. [[CrossRef](#)]
21. Mosqueira, D.; Mannhardt, I.; Bhagwan, J.R.; Lis-Slimak, K.; Katili, P.; Scott, E.; Hassan, M.; Prondzynski, M.; Harmer, S.C.; Tinker, A.; et al. CRISPR/Cas9 editing in human pluripotent stem cell-cardiomyocytes highlights arrhythmias, hypocontractility, and energy depletion as potential therapeutic targets for hypertrophic cardiomyopathy. *Eur. Heart J.* **2018**, *39*, 3879–3892. [[CrossRef](#)] [[PubMed](#)]
22. Ladha, F.A.; Thakar, K.; Pettinato, A.M.; Legere, N.; Cohn, R.; Romano, R.; Meredith, E.; Chen, Y.S.; Hinson, J.T. Identifying cardiac actinin interactomes reveals sarcomere crosstalk with RNA-binding proteins. *bioRxiv* **2020**, *2020*, 994004.
23. Wan, C.; Borgeson, B.; Phanse, S.; Tu, F.; Drew, K.; Clark, G.; Xiong, X.; Kagan, O.; Kwan, J.; Bezginov, A.; et al. Panorama of ancient metazoan macromolecular complexes. *Nature* **2015**, *525*, 339–344. [[CrossRef](#)] [[PubMed](#)]
24. Linnemann, A.; van der Ven, P.F.; Vakeel, P.; Albinus, B.; Simonis, D.; Bendas, G.; Schenk, J.A.; Micheel, B.; Kley, R.A.; Furst, D.O. The sarcomeric Z-disc component myopodin is a multiadapter protein that interacts with filamin and alpha-actinin. *Eur. J. Cell Biol.* **2010**, *89*, 681–692. [[CrossRef](#)]
25. Friedrich, F.W.; Wilding, B.R.; Reischmann, S.; Crocini, C.; Lang, P.; Charron, P.; Muller, O.J.; McGrath, M.J.; Vollert, I.; Hansen, A.; et al. Evidence for FHL1 as a novel disease gene for isolated hypertrophic cardiomyopathy. *Hum. Mol. Genet.* **2012**, *21*, 3237–3254. [[CrossRef](#)]

26. Friedrich, F.W.; Reischmann, S.; Schwalm, A.; Unger, A.; Ramanujam, D.; Munch, J.; Muller, O.J.; Hengstenberg, C.; Galve, E.; Charron, P.; et al. FHL2 expression and variants in hypertrophic cardiomyopathy. *Basic Res. Cardiol.* **2014**, *109*, 451. [[CrossRef](#)]
27. Hinson, J.T.; Chopra, A.; Nafissi, N.; Polacheck, W.J.; Benson, C.C.; Swist, S.; Gorham, J.; Yang, L.; Schafer, S.; Sheng, C.C.; et al. HEART DISEASE. Titin mutations in iPSCs define sarcomere insufficiency as a cause of dilated cardiomyopathy. *Science* **2015**, *349*, 982–986. [[CrossRef](#)]
28. Cuello, F.; Knaust, A.E.; Saleem, U.; Loos, M.; Raabe, J.; Mosqueira, D.; Laufer, S.; Schweizer, M.; van der Kraak, P.; Flenner, F.; et al. Impairment of the ER/mitochondria compartment in human cardiomyocytes with PLN p.Arg14del mutation. *EMBO Mol. Med.* **2021**, *13*, e13074. [[CrossRef](#)]
29. Feyen, D.A.M.; Perea-Gil, I.; Maas, R.G.C.; Harakalova, M.; Gavidia, A.A.; Arthur Ataam, J.; Wu, T.H.; Vink, A.; Pei, J.; Vadgama, N.; et al. Unfolded Protein Response as a Compensatory Mechanism and Potential Therapeutic Target in PLN R14del Cardiomyopathy. *Circulation* **2021**, *144*, 382–392. [[CrossRef](#)]
30. Davis, J.; Davis, L.C.; Correll, R.N.; Makarewich, C.A.; Schwaneckamp, J.A.; Moussavi-Harami, F.; Wang, D.; York, A.J.; Wu, H.; Houser, S.R.; et al. A Tension-Based Model Distinguishes Hypertrophic versus Dilated Cardiomyopathy. *Cell* **2016**, *165*, 1147–1159. [[CrossRef](#)]
31. Haywood, N.J.; Wolny, M.; Rogers, B.; Trinh, C.H.; Shuping, Y.; Edwards, T.A.; Peckham, M. Hypertrophic cardiomyopathy mutations in the calponin-homology domain of ACTN2 affect actin binding and cardiomyocyte Z-disc incorporation. *Biochem. J.* **2016**, *473*, 2485–2493. [[CrossRef](#)]
32. Dorsch, L.M.; Schuldt, M.; dos Remedios, C.G.; Schinkel, A.F.L.; de Jong, P.L.; Michels, M.; Kuster, D.W.D.; Brundel, B.; van der Velden, J. Protein Quality Control Activation and Microtubule Remodeling in Hypertrophic Cardiomyopathy. *Cells* **2019**, *8*, 741. [[CrossRef](#)]
33. Spaich, S.; Will, R.D.; Just, S.; Kuhn, C.; Frank, D.; Berger, I.M.; Wiemann, S.; Korn, B.; Koegl, M.; Backs, J.; et al. F-box and leucine-rich repeat protein 22 is a cardiac-enriched F-box protein that regulates sarcomeric protein turnover and is essential for maintenance of contractile function in vivo. *Circ. Res.* **2012**, *111*, 1504–1516. [[CrossRef](#)]
34. Lewis, Y.E.; Moskovitz, A.; Mutlak, M.; Heineke, J.; Caspi, L.H.; Kehat, I. Localization of transcripts, translation, and degradation for spatiotemporal sarcomere maintenance. *J. Mol. Cell. Cardiol.* **2018**, *116*, 16–28. [[CrossRef](#)]
35. Agarwal, R.; Paulo, J.A.; Toepfer, C.N.; Ewoldt, J.K.; Sundaram, S.; Chopra, A.; Zhang, Q.; Gorham, J.; DePalma, S.R.; Chen, C.S.; et al. Filamin C Cardiomyopathy Variants Cause Protein and Lysosome Accumulation. *Circ. Res.* **2021**, *129*, 751–766. [[CrossRef](#)]
36. Valdes-Mas, R.; Gutierrez-Fernandez, A.; Gomez, J.; Coto, E.; Astudillo, A.; Puente, D.A.; Reguero, J.R.; Alvarez, V.; Moris, C.; Leon, D.; et al. Mutations in filamin C cause a new form of familial hypertrophic cardiomyopathy. *Nat. Commun.* **2014**, *5*, 5326. [[CrossRef](#)]
37. Eijgenraam, T.R.; Boogerd, C.J.; Stege, N.M.; Oliveira Nunes Teixeira, V.; Dokter, M.M.; Schmidt, L.E.; Yin, X.; Theofilatos, K.; Mayr, M.; van der Meer, P.; et al. Protein Aggregation Is an Early Manifestation of Phospholamban p.(Arg14del)-Related Cardiomyopathy: Development of PLN-R14del-Related Cardiomyopathy. *Circ. Heart Fail.* **2021**, *4*, e008532. [[CrossRef](#)]
38. Arvanitis, M.; Tampakakis, E.; Zhang, Y.; Wang, W.; Auton, A.; Me Research, T.; Dutta, D.; Glavaris, S.; Keramati, A.; Chatterjee, N.; et al. Genome-wide association and multi-omic analyses reveal ACTN2 as a gene linked to heart failure. *Nat. Commun.* **2020**, *11*, 1122. [[CrossRef](#)]
39. Eschenhagen, T.; Carrier, L. Cardiomyopathy phenotypes in human-induced pluripotent stem cell-derived cardiomyocytes—a systematic review. *Pflug. Arch.* **2019**, *471*, 755–768. [[CrossRef](#)]
40. Brandao, K.O.; Tabel, V.A.; Atsma, D.E.; Mummery, C.L.; Davis, R.P. Human pluripotent stem cell models of cardiac disease: From mechanisms to therapies. *Dis. Model. Mech.* **2017**, *10*, 1039–1059. [[CrossRef](#)]
41. Puri, M.C.; Nagy, A. Concise review: Embryonic stem cells versus induced pluripotent stem cells: The game is on. *Stem Cells* **2012**, *30*, 10–14. [[CrossRef](#)]
42. Shibamiya, A.; Schulze, E.; Krauss, D.; Augustin, C.; Reinsch, M.; Schulze, M.L.; Steuck, S.; Mearini, G.; Mannhardt, I.; Schulze, T.; et al. Cell Banking of hiPSCs: A Practical Guide to Cryopreservation and Quality Control in Basic Research. *Curr. Protoc. Stem Cell Biol.* **2020**, *55*, e127. [[CrossRef](#)]
43. Breckwoldt, K.; Letuffe-Breniere, D.; Mannhardt, I.; Schulze, T.; Ulmer, B.; Werner, T.; Benzin, A.; Klampe, B.; Reinsch, M.C.; Laufer, S.; et al. Differentiation of cardiomyocytes and generation of human engineered heart tissue. *Nat. Protoc.* **2017**, *12*, 1177–1197. [[CrossRef](#)]
44. Skryabin, B.V.; Kummerfeld, D.-M.; Gubar, L.; Seeger, B.; Kaiser, H.; Stegemann, A.; Roth, J.; Meuth, S.G.; Pavenstädt, H.; Sherwood, J.; et al. Pervasive head-to-tail insertions of DNA templates mask desired CRISPR-Cas9-mediated genome editing events. *Sci. Adv.* **2020**, *6*, eaax2941. [[CrossRef](#)]
45. Mosqueira, D.; Lis-Slimak, K.; Denning, C. High-Throughput Phenotyping Toolkit for Characterizing Cellular Models of Hypertrophic Cardiomyopathy In Vitro. *Methods Protoc.* **2019**, *2*, 83. [[CrossRef](#)]
46. Patro, R.; Duggal, G.; Love, M.I.; Irizarry, R.A.; Kingsford, C. Salmon provides fast and bias-aware quantification of transcript expression. *Nat. Methods* **2017**, *14*, 417–419. [[CrossRef](#)]
47. Sonesson, C.; Love, M.I.; Robinson, M.D. Differential analyses for RNA-seq: Transcript-level estimates improve gene-level inferences. *F1000Research* **2015**, *4*, 1521. [[CrossRef](#)]

48. Love, M.I.; Huber, W.; Anders, S. Moderated estimation of fold change and dispersion for RNA-seq data with DESeq2. *Genome Biol.* **2014**, *15*, 550. [[CrossRef](#)]
49. Strimmer, K. fdrtool: A versatile R package for estimating local and tail area-based false discovery rates. *Bioinformatics* **2008**, *24*, 1461–1462. [[CrossRef](#)]
50. Wenzel, K.; Kramer, E.; Geertz, B.; Carrier, L.; Felix, S.B.; Konemann, S.; Schlossarek, S. A Transgenic Mouse Model of Eccentric Left Ventricular Hypertrophy With Preserved Ejection Fraction Exhibits Alterations in the Autophagy-Lysosomal Pathway. *Front. Physiol.* **2021**, *12*, 614878. [[CrossRef](#)]
51. Singh, S.R.; Meyer-Jens, M.; Alizoti, E.; Bacon, W.C.; Davis, G.; Osinska, H.; Gulick, J.; Reischmann-Düsener, S.; Orthey, E.; McLendon, P.M.; et al. A high-throughput screening identifies ZNF418 as a novel regulator of the ubiquitin-proteasome system and autophagy-lysosomal pathway. *Autophagy* **2020**, *17*, 3124–3139. [[CrossRef](#)] [[PubMed](#)]
52. Vignier, N.; Schlossarek, S.; Fraysse, B.; Mearini, G.; Kramer, E.; Pointu, H.; Mougenot, N.; Guiard, J.; Reimer, R.; Hohenberg, H.; et al. Nonsense-Mediated mRNA Decay and Ubiquitin-Proteasome System Regulate Cardiac Myosin-Binding Protein C Mutant Levels in Cardiomyopathic Mice. *Circ. Res.* **2009**, *105*, 239–248. [[CrossRef](#)] [[PubMed](#)]
53. Schlossarek, S.; Englmann, D.R.; Sultan, K.R.; Sauer, M.; Eschenhagen, T.; Carrier, L. Defective proteolytic systems in Mybpc3-targeted mice with cardiac hypertrophy. *Basic Res. Cardiol.* **2011**, *107*, 235. [[CrossRef](#)]
54. Suomi, T.; Elo, L.L. Enhanced differential expression statistics for data-independent acquisition proteomics. *Sci. Rep.* **2017**, *7*, 5869. [[CrossRef](#)] [[PubMed](#)]
55. Phipson, B.; Lee, S.; Majewski, I.J.; Alexander, W.S.; Smyth, G.K. Robust Hyperparameter Estimation Protects against Hypervariable Genes and Improves Power to Detect Differential Expression. *Ann. Appl. Stat.* **2016**, *10*, 946–963. [[CrossRef](#)]
56. Benjamini, Y.; Hochberg, Y. Controlling the False Discovery Rate: A Practical and Powerful Approach to Multiple Testing. *J. R. Stat. Soc. Ser. B* **1995**, *57*, 289–300. [[CrossRef](#)]
57. Zhou, C.; Zhong, W.; Zhou, J.; Sheng, F.; Fang, Z.; Wei, Y.; Chen, Y.; Deng, X.; Xia, B.; Lin, J. Monitoring autophagic flux by an improved tandem fluorescently tagged LC3 (mTagRFP-mWasabi-LC3) reveals that high-dose rapamycin impairs autophagic flux in cancer cells. *Autophagy* **2012**, *8*, 1215–1226. [[CrossRef](#)]
58. Wasilko, D.J.; Lee, S.E.; Stutzman-Engwall, K.J.; Reitz, B.A.; Emmons, T.L.; Mathis, K.J.; Bienkowski, M.J.; Tomasselli, A.G.; Fischer, H.D. The titerless infected-cells preservation and scale-up (TIPS) method for large-scale production of NO-sensitive human soluble guanylate cyclase (sGC) from insect cells infected with recombinant baculovirus. *Protein Expr. Purif.* **2009**, *65*, 122–132. [[CrossRef](#)]

Supplement

Supplemental Figures

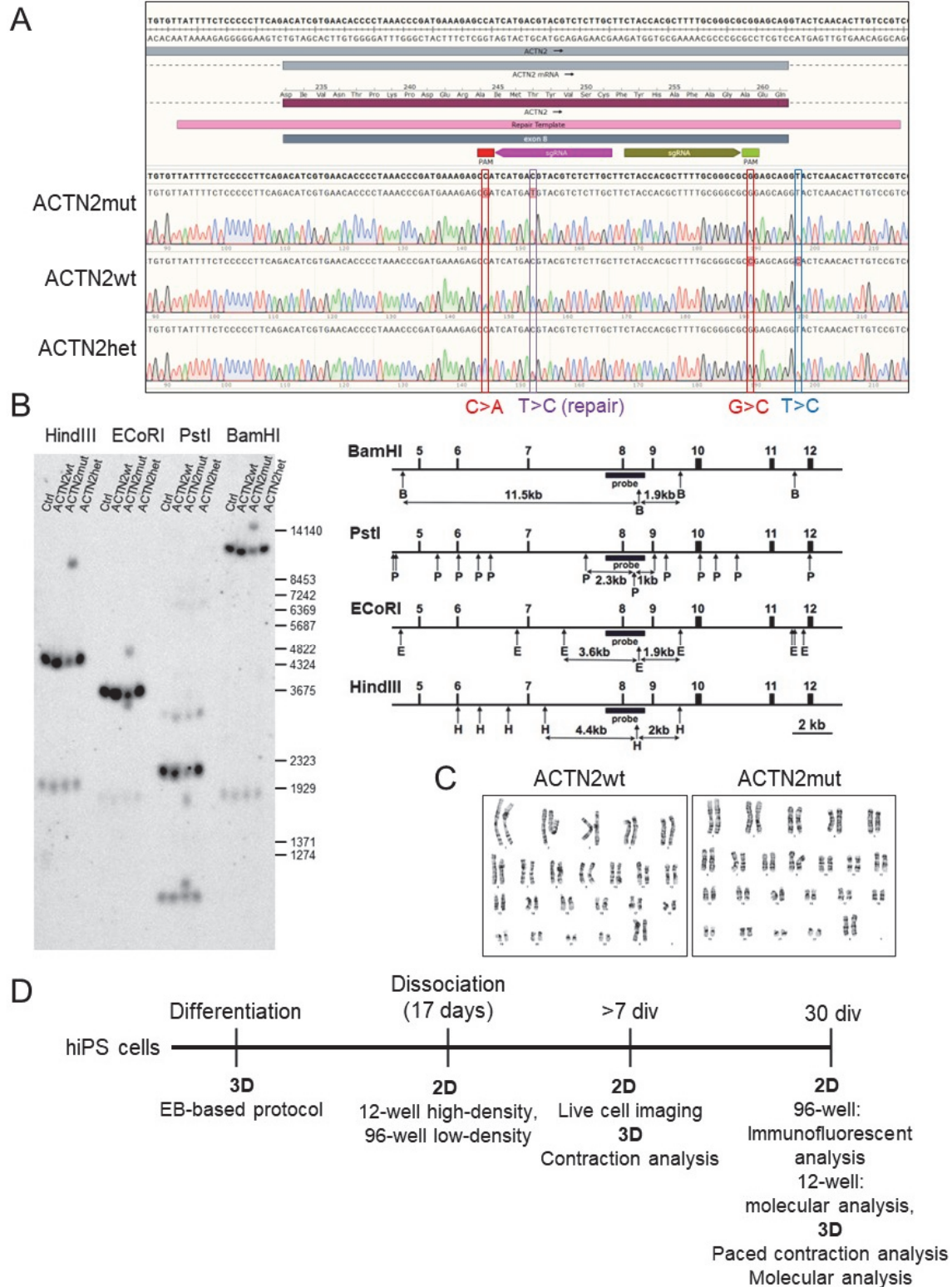


Figure S1. Generation of the ACTN2wt and ACTN2mut hiPSC lines. (A) Sanger sequencing results of the affected *ACTN2* locus in exon 8, with the location of the PAM

sequences, sgRNAs and repair template used to create the ACTN2wt and ACTN2mut hiPSC lines from the heterozygous ACTN2het hiPSC line. At position 152 is indicated the heterozygous c.740C>T mutation in ACTN2het (purple). ACTN2wt sequence shows the repair at position 152 (p.740C; ACG; pThr247; purple), the two introduced silent mutations (heterozygous G>A at position 144 and homozygous G>C at position 189; red) and the on-target effect of CRISPR/Cas at position 197; blue), which induced the skipping of exon 8 and a nonsense mRNA. ACTN2mut sequence shows the mutation at position 152 (p.740T, ATG; pMet247) and no silent mutations, suggesting the presence of only one mutant allele at the locus. **(B)** Southern blot performed with 4 different restriction enzymes on genomic DNA extracted from ACTN2wt, ACTN2mut, ACTN2het and a control (Ctrl) hiPSC line. This reveals a large re-arrangement of one allele in ACTN2mut, affecting the 5' fragment of all restriction enzymes, leading to a nonsense mRNA. **(C)** G-banding results are depicted by representative karyograms of the investigated hiPSC ACTN2wt (passage 55) and ACTN2wt (passage 68) lines. **(C)** Protocol for the production of hiPSC-derived cardiomyocytes, models and experimental procedures that were used for this study. Abbreviations: div, days in vitro; EB, embryoid body.

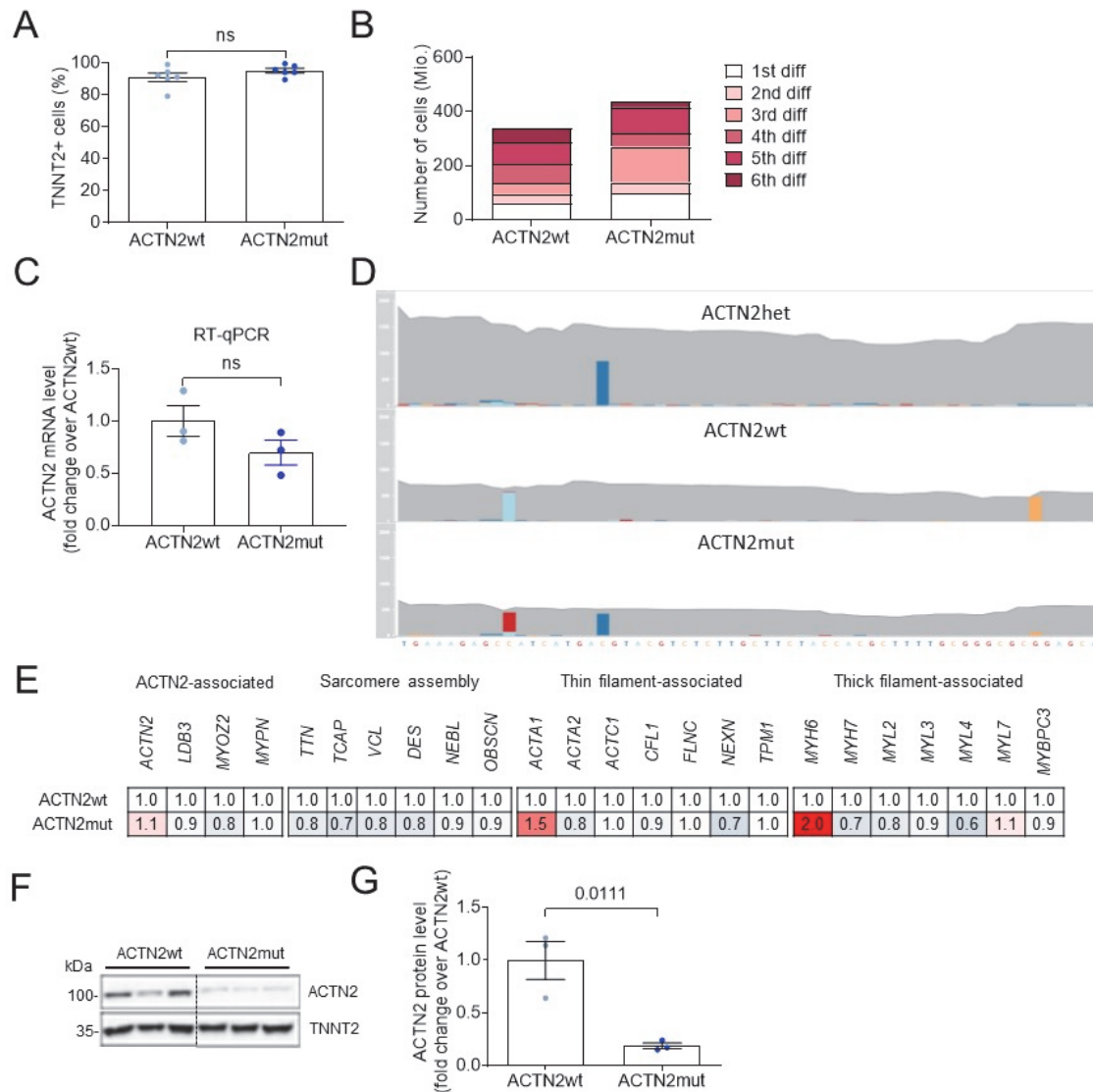


Figure S2: Validation of cardiac differentiation and mRNA and protein analysis. (A) Percentage of TNNT2+ cells in ACTN2wt and ACTN2mut hiPSC-CMs was determined by flow cytometry to validate the quality of cardiac differentiation (n = 6 differentiations). (B) Cardiomyocyte yield of six single differentiation runs was evaluated in ACTN2wt and ACTN2mut hiPSC-CMs. (C) Quantification of *ACTN2* mRNA by RT-qPCR with the housekeeping gene *GAPDH*. (D) RNA-seq of *ACTN2* locus showing 2-fold lower RNA counts in both ACTN2wt and ACTN2mut compared to the original heterozygous ACTN2-mutated (ACTN2het; c.740C>T, dark blue) hiPSC line (red to light blue (C>A) and orange (G>C), silent mutations in ACTN2wt). (E) Gene expression analysis were performed with the nanoString nCounter® Elements technology. The mRNA counts were normalized to housekeeping genes *ABCF1*, *CLTC*, *GAPDH*, *TUBB* and related to ACTN2wt (ACTN2wt: N/n=18/3, ACTN2mut: N/n=17/3). (F) Representative Western is shown performed on SDS-fraction of pooled samples of hiPSC-CMs stained with antibodies against ACTN2 and TNNT2 and (G) corresponding quantification of ACTN2 normalized to TNNT2 is shown (ACTN2wt: n/d = 3/1, ACTN2mut: n/d = 3/1). Data are expressed as mean \pm SEM, and P-values were obtained with the unpaired Student's t-test. Abbreviations: TNNT2, cardiac troponin T; kDa, kilodalton; N/n/d, number of (pooled) cells/wells/differentiations.

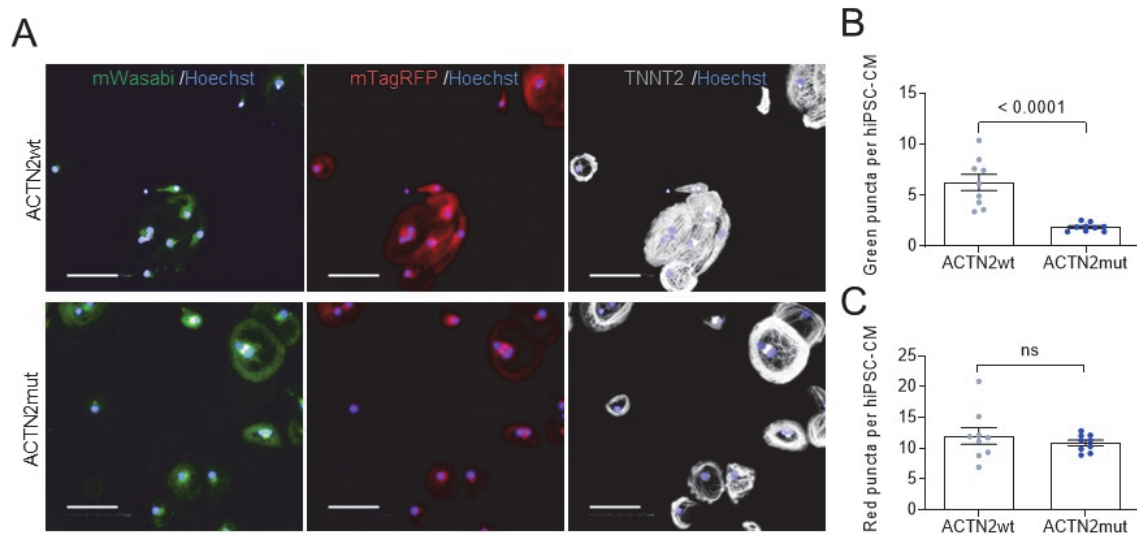


Figure S3. Representative data of the high-content screening performed in 2D-cultured hiPSC-CMs. (A) Representative images of the high-content imaging of ACTN2wt and ACTN2mut hiPSC-CMs transduced with an AAV6-mWasabi-mTagRFP-hLC3 tandem construct (MOI 10,000) on day 30 of culture. Subsequently, the hiPSC-CMs were fixed and stained with a TNNT2 (cardiac troponin T) antibody and Hoechst for nuclei staining. Representative images were taken with the Operetta high-content imaging system at 20x magnification (PerkinElmer; Scale bar = 100 μ m). (B) Number of green puncta and (C) number of red puncta per ACTN2wt and ACTN2mut hiPSC-CM (n=wells/treatment per CM per well: ACTN2wt (n=9); ACTN2mut (n=9)). Data are expressed as mean \pm SEM, with *P*-values obtained with the unpaired Student's t-test (panels B, C).

Supplementary Tables

Table S1. RNA-seq and mass spectrometry analyses of sarcomere-associated proteins in 2D-cultured ACTN2mut vs. ACTN2wt hiPSC-CMs.

Cell line	Group	RNA	Log2 ratio	FC	P-value	Adjusted P-value	Group	Protein	Log2 ratio	FC	P-value	Adjusted P-value
ACTN2mut vs ACTN2wt	Sarcomere-associated	<i>ACTA1</i>	0.84	1.78	6.98E-02	4.42E-01	Sarcomere-associated	<i>ACTA1</i>	-0.59	0.66	6.30E-06	2.93E-04
		<i>ACTC1</i>	0.26	1.20	2.69E-01	8.56E-01		<i>ACTC1</i>	-0.64	0.64	3.27E-03	4.84E-02
		<i>ACTN1</i>	-0.26	0.84	6.57E-01	9.83E-01		<i>ACTN1</i>	0.48	1.39	2.63E-05	9.58E-04
		<i>ACTN2</i>	0.46	1.38	2.14E-01	8.02E-01		<i>ACTN2</i>	-1.63	0.32	3.02E-80	2.91E-77
		<i>DES</i>	-0.01	0.99	9.75E-01	9.97E-01		<i>DES</i>	0.31	1.24	7.03E-02	3.34E-01
		<i>DMD</i>	-0.40	0.76	2.54E-01	8.44E-01		<i>DMD</i>	-0.21	0.87	2.10E-02	1.70E-01
		<i>FHL1</i>	-0.19	0.88	7.31E-01	9.87E-01		<i>FHL1</i>	0.56	1.47	1.34E-02	1.30E-01
		<i>FHL2</i>	-0.44	0.74	4.49E-02	3.37E-01		<i>FHL2</i>	0.27	1.20	3.74E-02	2.37E-01
		<i>FLNC</i>	0.33	1.25	1.71E-01	7.26E-01		<i>FLNC</i>	-0.49	0.71	3.94E-21	1.42E-18
		<i>JUP</i>	-0.06	0.96	8.18E-01	9.96E-01		<i>JUP</i>	-0.31	0.80	5.19E-06	2.54E-04
		<i>LDB3</i>	0.21	1.15	6.18E-01	9.80E-01		<i>LDB3</i>	0.01	1.01	1.00E+00	1.00E+00
		<i>MYBPC3</i>	0.35	1.27	3.94E-01	9.33E-01		<i>MYBPC3</i>	-0.82	0.57	4.61E-51	3.32E-48
		<i>MYH6</i>	0.92	1.89	2.95E-02	2.56E-01		<i>MYH6</i>	-0.52	0.70	3.35E-02	2.23E-01
		<i>MYH7</i>	-0.01	0.99	9.75E-01	9.97E-01		<i>MYH7</i>	-0.89	0.54	1.23E-10	1.54E-08
		<i>MYL1</i>	0.85	1.81	3.44E-01	9.11E-01		<i>MYL1</i>	-0.81	0.57	2.17E-115	3.13E-112
		<i>MYL2</i>	-0.03	0.98	9.49E-01	9.96E-01		<i>MYL2</i>	-0.65	0.64	5.23E-03	6.92E-02
		<i>MYL3</i>	0.03	1.02	9.11E-01	9.96E-01		<i>MYL3</i>	-0.68	0.62	2.10E-09	2.33E-07
		<i>MYL4</i>	-0.32	0.80	2.06E-01	7.88E-01		<i>MYL4</i>	-0.58	0.67	1.31E-06	7.15E-05
		<i>MYOM1</i>	0.06	1.04	8.56E-01	9.96E-01		<i>MYOM1</i>	-0.99	0.50	1.80E-05	7.01E-04
		<i>MYOZ2</i>	-0.07	0.95	8.09E-01	9.96E-01		<i>MYOZ2</i>	-1.00	0.50	5.66E-42	3.26E-39
<i>MYPN</i>	0.32	1.25	5.26E-01	9.72E-01	<i>MYPN</i>	-0.24	0.84	1.91E-15	4.59E-13			

		<i>NEBL</i>	-0.14	0.90	6.14E-01	9.80E-01		<i>NEBL</i>	-0.63	0.65	9.34E-21	2.99E-18
		<i>OBSCN</i>	0.15	1.11	7.25E-01	9.87E-01		<i>OBSCN</i>	-0.72	0.61	8.78E-22	3.62E-19
		<i>OBSL1</i>	0.51	1.42	1.51E-01	6.88E-01		<i>OBSL1</i>	-0.24	0.85	2.36E-01	6.25E-01
		<i>PKP2</i>	0.13	1.10	6.45E-01	9.83E-01		<i>PKP2</i>	-0.55	0.68	9.08E-05	2.73E-03
		<i>SLMAP</i>	-0.34	0.79	2.04E-01	7.84E-01		<i>SLMAP</i>	-0.21	0.86	9.36E-02	3.92E-01
		<i>SYNPO2</i>	0.37	1.29	4.28E-01	9.43E-01		<i>SYNPO2</i>	-0.40	0.76	1.78E-02	1.54E-01
		<i>SYNPO2L</i>	0.02	1.01	9.59E-01	9.96E-01		<i>SYNPO2L</i>	-0.69	0.62	3.31E-07	2.33E-05
		<i>TNNC1</i>	-0.09	0.94	6.90E-01	9.84E-01		<i>TNNC1</i>	-0.89	0.54	2.12E-08	1.91E-06
		<i>TNNI1</i>	0.44	1.36	1.17E-01	6.03E-01		<i>TNNI1</i>	-0.87	0.55	8.09E-07	4.67E-05
		<i>TNNI3</i>	0.15	1.11	5.12E-01	9.70E-01		<i>TNNI3</i>	-0.82	0.57	4.57E-05	1.54E-03
		<i>TNNT2</i>	0.22	1.17	3.50E-01	9.16E-01		<i>TNNT2</i>	-0.86	0.55	3.74E-07	2.51E-05
		<i>TPM1</i>	0.07	1.05	7.44E-01	9.91E-01		<i>TPM1</i>	-0.80	0.57	9.28E-14	1.78E-11
		<i>TPM3</i>	-0.23	0.86	6.77E-01	9.83E-01		<i>TPM3</i>	-0.93	0.52	4.17E-02	2.49E-01
		<i>TTN</i>	-0.14	0.90	7.64E-01	9.93E-01		<i>TTN</i>	-0.83	0.56	0.00E+00	3.60E-306

Purple indicates significantly altered genes or proteins. Abbreviation: FC, Fold change.

Table S2. RNA-seq and mass spectrometry analyses of the UPS and ALP in 2D-cultured ACTN2mut vs. ACTN2wt hiPSC-CMs.

Cell line	Group	RNA	Log2 ratio	FC	P-value	Adjusted P-value	Group	Protein	Log2 ratio	FC	P-value	Adjusted P-value
ACTN2mut vs ACTN2wt	UPS and ALP	<i>BNIP3</i>	1.85	3.61	0.0006	6.16E-03	UPS and ALP	ASAHI	0.89	1.85	2.29E-05	8.68E-04
		<i>CTSH</i>	1.13	2.18	0.0000	6.25E-05		BAG3	0.38	1.30	2.30E-02	1.79E-01
		<i>DEPTOR</i>	-1.74	0.30	0.0016	1.75E-02		CTSC	0.67	1.59	1.39E-03	2.61E-02
		<i>KLHL13</i>	-1.35	0.39	0.0000	1.93E-04		CTSL	1.07	2.10	2.26E-03	3.76E-02
		<i>MAP1LC3A</i>	-0.94	0.52	0.0246	2.23E-01		FAM98A	1.38	2.61	1.68E-02	1.50E-01
		<i>MDM2</i>	-0.95	0.52	0.0002	1.32E-03		GBA	0.38	1.30	4.71E-02	2.69E-01
		<i>STAT1</i>	-1.06	0.48	0.0463	3.44E-01		HSPA1A	0.23	1.18	2.37E-03	3.89E-02
		<i>TRIM4</i>	-6.35	0.01	0.0000	4.38E-07		PSMA3	0.38	1.30	1.97E-02	1.62E-01
								PSMA6	0.37	1.29	6.47E-04	1.47E-02
								PSMB5	0.45	1.37	3.68E-02	2.35E-01
								PSMC6	0.29	1.22	2.02E-03	3.42E-02
								PSMD11	0.31	1.24	1.11E-03	2.15E-02
								PSME1	0.46	1.37	5.36E-06	2.54E-04
								PSME2	0.38	1.30	3.78E-02	2.39E-01
								TRIM54	0.44	1.36	2.60E-03	4.10E-02
								UBA1	0.39	1.31	7.83E-07	4.67E-05
								UBE2O	0.68	1.60	2.53E-02	1.88E-01
								UBQLN2	0.70	1.62	7.99E-04	1.70E-02

Purple indicates significantly altered genes or proteins. Abbreviation: FC, Fold change.

Table S3. RNA-seq and mass spectrometry analyses of sarcomere-associated proteins in 3D-cultured ACTN2mut vs. ACTN2wt hiPSC-CMs (EHTs).

Cell line	Group	RNA	Log2 ratio	FC	P-value	Adjusted P-value	Group	Protein	Log2 ratio	FC	P-value	Adjusted P-value
ACTN2mut vs ACTN2wt	Sarcomere-associated	<i>ACTA1</i>	2.79	6.91	6.13E-05	9.47E-02	Sarcomere-associated	<i>ACTA1</i>	-0.55	0.69	1.30E-04	1.63E-02
		<i>ACTC1</i>	0.71	1.64	2.41E-04	1.74E-01		<i>ACTC1</i>	-0.47	0.72	6.47E-02	1.00E+00
		<i>ACTN1</i>	0.38	1.30	1.18E-01	9.04E-01		<i>ACTN1</i>	0.03	1.02	1.00E+00	1.00E+00
		<i>ACTN2</i>	0.10	1.07	6.47E-01	9.94E-01		<i>ACTN2</i>	-1.41	0.38	1.14E-56	1.65E-53
		<i>DES</i>	0.61	1.53	1.41E-02	6.46E-01		<i>DES</i>	-0.42	0.75	8.26E-07	1.40E-04
		<i>DMD</i>	-0.14	0.91	5.65E-01	9.91E-01		<i>DMD</i>	-0.15	0.90	1.00E+00	1.00E+00
		<i>FHL1</i>	-0.04	0.97	9.49E-01	9.99E-01		<i>FHL1</i>	-0.43	0.74	2.81E-01	1.00E+00
		<i>FHL2</i>	0.09	1.06	7.03E-01	9.95E-01		<i>FHL2</i>	-0.14	0.91	8.59E-01	1.00E+00
		<i>FLNC</i>	0.70	1.63	2.72E-02	7.50E-01		<i>FLNC</i>	-0.09	0.94	1.00E+00	1.00E+00
		<i>JUP</i>	-0.31	0.81	9.16E-02	8.80E-01		<i>JUP</i>	-0.63	0.65	2.91E-12	1.20E-09
		<i>LDB3</i>	-0.07	0.95	6.90E-01	9.95E-01		<i>LDB3</i>	-0.44	0.74	7.13E-05	1.00E-02
		<i>MYBPC3</i>	0.20	1.15	2.87E-01	9.70E-01		<i>MYBPC3</i>	-0.94	0.52	9.00E-49	8.65E-46
		<i>MYH6</i>	0.43	1.35	1.52E-01	9.23E-01		<i>MYH6</i>	-0.29	0.82	3.75E-03	2.17E-01
		<i>MYH7</i>	0.04	1.03	8.86E-01	9.97E-01		<i>MYH7</i>	-0.95	0.52	1.16E-01	1.00E+00
		<i>MYL1</i>	1.11	2.15	3.21E-01	9.75E-01		<i>MYL1</i>	-0.74	0.60	7.06E-94	2.04E-90
		<i>MYL2</i>	-0.18	0.88	5.62E-01	9.90E-01		<i>MYL2</i>	-0.84	0.56	1.55E-02	5.40E-01
		<i>MYL3</i>	-0.35	0.78	1.18E-01	9.04E-01		<i>MYL3</i>	-0.69	0.62	1.54E-08	4.92E-06
		<i>MYL4</i>	-0.29	0.82	1.69E-01	9.36E-01		<i>MYL4</i>	-0.56	0.68	1.14E-07	2.52E-05
		<i>MYOM1</i>	0.28	1.21	1.79E-01	9.38E-01		<i>MYOM1</i>	-1.01	0.50	5.87E-04	5.46E-02
		<i>MYOZ2</i>	-0.56	0.68	1.47E-03	3.39E-01		<i>MYOZ2</i>	-1.01	0.50	3.52E-39	2.54E-36
<i>MYPN</i>	-0.01	0.99	9.55E-01	9.99E-01	<i>MYPN</i>	-0.56	0.68	3.72E-11	1.34E-08			
<i>NEBL</i>	-0.12	0.92	5.48E-01	9.90E-01	<i>NEBL</i>	-0.54	0.69	8.10E-07	1.40E-04			

		<i>OBSCN</i>	0.22	1.17	2.42E-01	9.64E-01		<i>OBSCN</i>	-0.35	0.79	3.44E-04	3.54E-02
		<i>OBSL1</i>	0.29	1.23	9.31E-02	8.81E-01		<i>OBSL1</i>	-0.06	0.96	1.00E+00	1.00E+00
		<i>PKP2</i>	-0.37	0.78	6.96E-02	8.44E-01		<i>PKP2</i>	-0.65	0.64	1.70E-08	4.92E-06
		<i>SLMAP</i>	-0.10	0.94	6.47E-01	9.94E-01		<i>SLMAP</i>	-0.39	0.76	1.08E-01	1.00E+00
		<i>SYNPO2</i>	-0.51	0.70	1.78E-01	9.38E-01		<i>SYNPO2</i>	-0.79	0.58	4.08E-06	6.19E-04
		<i>SYNPO2L</i>	0.04	1.03	8.38E-01	9.97E-01		<i>SYNPO2L</i>	-0.76	0.59	1.54E-07	3.17E-05
		<i>TNNC1</i>	-0.53	0.69	1.42E-02	6.46E-01		<i>TNNC1</i>	-0.87	0.55	1.13E-06	1.81E-04
		<i>TNNI1</i>	-0.02	0.99	9.22E-01	9.99E-01		<i>TNNI1</i>	-0.81	0.57	3.52E-07	6.77E-05
		<i>TNNI3</i>	-0.19	0.88	5.84E-01	9.92E-01		<i>TNNI3</i>	-0.75	0.60	4.00E-03	2.26E-01
		<i>TNNT2</i>	-0.13	0.91	4.76E-01	9.88E-01		<i>TNNT2</i>	-0.84	0.56	1.04E-07	2.51E-05
		<i>TPM1</i>	-0.17	0.89	3.68E-01	9.75E-01		<i>TPM1</i>	-0.70	0.62	8.46E-13	4.07E-10
		<i>TPM3</i>	-0.41	0.75	7.99E-02	8.62E-01		<i>TPM3</i>	-0.80	0.58	6.25E-01	1.00E+00
		<i>TTN</i>	0.01	1.01	9.53E-01	9.99E-01		<i>TTN</i>	-0.05	0.96	1.00E+00	1.00E+00

Purple indicates significantly altered genes or proteins. Abbreviation: FC, Fold change.

Table S4. Acronyms and names of genes evaluated with the nanoString nCounter® Elements technology.

Gene	Acronym	Accession number (NCBI)
Alpha-Actinin 2	<i>ACTN2</i>	NM_001103.2
LIM Domain Binding 3	<i>LDB3</i>	NM_001080116.1
Myozenin 2	<i>MYOZ2</i>	NM_016599.4
Myopalladin	<i>MYPN</i>	NM_032578.2
Titin	<i>TTN</i>	NM_133432.1
Titin-cap	<i>TCAP</i>	NM_003673.3
Vinculin	<i>VCL</i>	NM_014000.2
Desmin	<i>DES</i>	NM_001927.3
Nebulin	<i>NEBL</i>	NM_001173484.1
Obscurin	<i>OBSCN</i>	NM_001098623.2
Actin alpha 1, skeletal muscle	<i>ACTA1</i>	NM_001100.3
Actin Alpha 2, smooth muscle	<i>ACTA2</i>	NM_001613.1
Actin alpha, cardiac muscle 1	<i>ACTC1</i>	NM_005159.4
Cofilin 1	<i>CFL1</i>	NM_005507.2
Filamin C	<i>FLNC</i>	NM_001127487.1
Nexilin	<i>NEXN</i>	NM_144573.3
Tropomyosin 1	<i>TPM1</i>	NM_000366.5
Myosin heavy chain 6	<i>MYH6</i>	NM_002471.3
Myosin heavy chain 7	<i>MYH7</i>	NM_000257.2
Myosin Regulatory Light Chain 2	<i>MYL2</i>	NM_000432.3
Myosin Regulatory Light Chain 3	<i>MYL3</i>	NM_000258.2
Myosin Regulatory Light Chain 4	<i>MYL4</i>	NM_002476.2
Myosin Regulatory Light Chain 7	<i>MYL7</i>	NM_021223.2
Cardiac myosin binding protein C	<i>MYBPC3</i>	NM_000256.3
ATP Binding Cassette Subfamily F Member 1	<i>ABCF1</i>	NM_001090.2
Clathrin Heavy Chain	<i>CLTC</i>	NM_004859.2
Glyceraldehyde 3-phosphate dehydrogenase	<i>GAPDH</i>	NM_002046.3
Tubulin Beta Class I	<i>TUBB</i>	NM_178014.3

Table S5. LC-MS/MS parameter (data dependent mode, spectral library).

Data dependent analyses (DDA)	
Reversed phase liquid chromatography	Ultimate 3000 RSLC (Thermo Scientific)
<i>Trap column</i>	75 μm inner diameter, packed with 3 μm C18 particles (Acclaim PepMap100, Thermo Scientific)
<i>Analytical column</i>	Accucore™ 150-C18, 25 cm x 75 μm , 2.6 μm C18, 150 Å (Thermo Scientific)
<i>Flow rate</i>	300 nl/min
<i>Column oven temperature</i>	40 °C
<i>Buffer system</i>	Binary buffer system consisting of 0.1% acetic acid in HPLC-grade water (buffer A) and 100% ACN in 0.1% acetic acid (buffer B)
<i>Gradient</i>	Gradient of buffer B: 2 min 2% to 5 %, 10 min 5%, 120 min 5% to 25%, 5 min 25% to 40%, 2 min 40% to 90%, 5 min 90%, 3 min 90% to 2%, 10 min 2%
Mass spectrometer	Q Exactive HFX
<i>Operation mode</i>	Data-dependent
<i>Electrospray</i>	Nanospray Flex Ion Source
Full MS	
<i>MS scan resolution</i>	60,000
<i>AGC target</i>	3.00E+06
<i>Maximum ion injection time for the MS scan</i>	45 ms
<i>Scan range</i>	350 to 1650 m/z
<i>Spectra data type</i>	Profile
dd-MS2	
<i>Resolution</i>	15,000
<i>MS/MS AGC target</i>	1.00E+05
<i>Maximum ion injection time for the MS/MS scans</i>	22 ms
<i>Spectra data type</i>	Profile
<i>Selection for MS/MS</i>	12 most abundant isotope patterns with charge ≥ 2 from the survey scan
<i>Isolation window</i>	1,3 m/z
<i>Fixed first mass</i>	100 m/z
<i>Dissociation mode</i>	HCD
<i>Normalized collision energy</i>	27%
<i>Dynamic exclusion</i>	45 s
<i>Charge exclusion</i>	1,>6

Table S6. LC-MS/MS parameter (data independent mode; quantitative data).

Data independent analyses (DIA)	
Reversed phase liquid chromatography	Ultimate 3000 RSLC (Thermo Scientific)
<i>Trap column</i>	75 μ m inner diameter, packed with 3 μ m C18 particles (Acclaim PepMap100, Thermo Scientific)
<i>Analytical column</i>	Accucore™ 150-C18, 25 cm x 75 μ m, 2.6 μ m C18, 150 Å (Thermo Scientific)
<i>Flow rate</i>	300 nl/min
<i>Column oven temperature</i>	40 °C
<i>Buffer system</i>	Binary buffer system consisting of 0.1% acetic acid in HPLC-grade water (buffer A) and 100% ACN in 0.1% acetic acid (buffer B)
<i>Gradient</i>	Dradient of buffer B: 2 min 22% to 5 %, 8 min 5%, 120 min 5% to 25%, 5 min 25 to 40%, 2 min 40% to 90%, 5 min 90%, 3 min 90% to 2%, 10 min 2%
Mass spectrometer	Q Exactive HFX
<i>Operation mode</i>	Data-independent
<i>Electrospray</i>	Nanospray Flex Ion Source
Full MS	
<i>MS scan resolution</i>	120,000
<i>AGC target</i>	3.00E+06
<i>Maximum ion injection time for the MS scan</i>	60 ms
<i>Scan range</i>	350 to 1200 <i>m/z</i>
<i>Spectra data type</i>	Profile
DIA MS2	
<i>Resolution</i>	30,000
<i>MS/MS AGC target</i>	3.00E+06
<i>Maximum ion injection time for the MS/MS scans</i>	Auto
<i>Spectra data type selection for MS/MS</i>	Profile
<i>Isolation window</i>	1
<i>Fixed first mass</i>	70 windows <i>m/z</i> 10, 11 <i>m/z</i>
<i>Dissociation mode</i>	200
<i>Normalized collision energy</i>	Higher energy collisional dissociation (HCD)
<i>Dissociation mode</i>	27.5%
	HCD

Video legends

Video 1. Contracting ACTN2wt hiPSC-CMs transduced with WT-ACTN2 HaloTag.

Widefield fluorescence microscopy of contracting ACTN2wt hiPSC-CMs that were transduced with AAV6-*TNNT2*-WT-*ACTN2*-HaloTag and stained for imaging with TMR-ligand to visualize sarcomeres.

Video 2. Contracting ACTN2wt hiPSC-CMs transduced with MUT-ACTN2 HaloTag.

Widefield fluorescence microscopy of contracting ACTN2wt hiPSC-CMs that were transduced with AAV6-*TNNT2*-MUT-*ACTN2*-HaloTag and stained for imaging with TMR-ligand to visualize sarcomeres.

Video 3. Contracting ACTN2wt EHTs. Widefield video microscopy of contracting ACTN2wt EHTs that were paced at 1 Hz to analyze functional parameters independent of varying baseline frequencies.

Video 4. Contracting ACTN2mut EHTs. Widefield video microscopy of contracting ACTN2mut EHTs that were paced at 1 Hz to analyze functional parameters independent of varying baseline frequencies.

Dataset legends

Dataset S1. MS data of 2D ACTN2mut hiPSC-CMs analyzed with IPA. Significantly altered proteins were submitted to an unsupervised analysis of ACTN2mut in relation to ACTN2wt hiPSC-CMs. Fisher's exact test, unadjusted P -value <0.05 .

Dataset S2. RNA-seq data of 2D ACTN2mut hiPSC-CMs analyzed with IPA. Significantly altered protein-coding genes were submitted to an unsupervised analysis of ACTN2mut in relation to ACTN2wt hiPSC-CMs. Fisher's exact test, unadjusted P -value <0.05 .

Supplemental experimental procedures

Ethics statement

The HCM patient carrying the *ACTN2* (c.740C>T; dbSNP ID: rs755492182) mutation was recruited in the outpatient HCM clinic at the University Heart and Vascular Center Hamburg and provided written informed consent for genetic analysis and the use of skin fibroblasts [1]. All procedures were in accordance with the Code of Ethics of the World Medical Association (Declaration of Helsinki). The study was reviewed and approved by the Ethical Committee of the Ärztekammer Hamburg (PV3501).

Generation and culture of hiPSC-derived cardiomyocytes (hiPSC-CMs) in 2D and EHT formats

Generation of both wild-type (*ACTN2*^{wt}) and mutant (*ACTN2*^{mut}) hiPSC lines was performed with CRISPR/Cas9 gene tools in *ACTN2*^{het} hiPSC [1]. Both clones were analyzed for the same off-targets as published previously. Additionally, PCR fragments of cells containing the modified *ACTN2* locus were subcloned using the CloneJET PCR Cloning Kit (Thermo Scientific, Vilnius, Lithuania) for discrimination of allele-specific genotypes. Finally, all used cell lines were genotyped by PCR for the *ACTN2* locus and karyotyped by G-banding as reported previously [1]. To amplify specific DNA fragments, PCR was conducted according to standard protocols using PrimeSTAR® HS DNA Polymerase (Takara, Kusatsu, Japan) and AmpliTaq® Gold DNA polymerase (Thermo Fisher Scientific, Vilnius, Lithuania) following manufacturer's instructions.

Cardiomyocyte (CM) differentiation from hiPSCs was performed following a three-step protocol with generation of embryoid bodies (EBs) in spinner flasks and cardiac differentiation efficiency was determined by flow cytometry as described previously [2]. After dissociation with collagenase 2 (200 units/mL, LS004176, Worthington, Lakewood, NJ) hiPSC-CMs were plated on Geltrex-coated (1:100, Gibco, Grand Island, NY) 96-well or 12-well plates at a density of 2,500 - 5,000 cells/well or 440,000 cells/well, respectively. HiPSC-CMs were maintained in culture for 7 days in 96-well plates (µclear®, Greiner Bio-One, Frickenhausen, Germany) when used for live cell imaging and for 30 days for immunofluorescent analysis, as well as 12-well plates, which were used for molecular analysis, at 37 °C in 7% CO₂ and atmospheric O₂ (21%) prior to further analysis. Furthermore, single cell suspensions of hiPSC-CMs were subjected to the 3D format of EHTs, which were generated in a 24-well format (800,000 hiPSC-CM/EHT) in a fibrin matrix, maintained in culture and analyzed from day 26 on as described previously [1].

Southern blot DNA analysis

Southern blot was performed as previously described [3]. HiPSC pellets were lysed in buffer containing 100 mM tris-HCl (pH 8.5), 5 mM EDTA, 0.2% SDS, 200 mM NaCl, and proteinase K (100 µg/ml; Roche) overnight at 55 °C. Genomic DNA was extracted by phenol-chloroform and chloroform, followed by precipitation with 2.5 volumes of isopropanol and washing with 70% ethanol. The DNA pellet was dissolved in TE buffer [10 mM tris (pH 7.9) and 0.2 mM EDTA]. Approximately 10 to 20 µg of genomic DNA was digested with the corresponding restriction endonuclease, fractionated on 0.8% agarose gels, and transferred to GeneScreen nylon membranes (NEN DuPont). The membranes were hybridized with ³²P-labeled specific DNA probe. DNA labeling was performed using a random prime DNA labeling kit (Roche) and [α -³²P] deoxycytidine-5' triphosphate (PerkinElmer). Membranes were washed with 0.5x saline sodium

phosphate EDTA (SSPE) buffer [1× saline sodium phosphate EDTA buffer is 0.18 M NaCl, 10 mM NaH₂PO₄, and 1 mM EDTA (pH 7.7)] and 0.5% SDS at 65 °C and exposed to MS film (Kodak) at –80 °C.

Immunofluorescence staining of hiPSC-CMs

HiPSC-CMs were cultured for 30 days in 96-well plates (μ clear®, Greiner Bio-One, Frickenhausen, Germany) and subsequently prepared for immunofluorescence analysis as described previously [1]. The following primary antibodies were used: ACTN2 – A7811 (1:800), Sigma-Aldrich, St.Louis, MO; cardiac troponin T (TNNT2) – ab8295 (1:200) or ab45932 (1:500), Abcam, Cambridge, UK; HaloTag – G9281 (1:400), Promega, Madison, WI. The following secondary antibodies were used: anti-mouse Alexa Fluor® 488 antibody - LT A11029 (1:800), Life Technologies, Eugene, OR; anti-rabbit Alexa Fluor® 546 antibody - LT A11035 (1:800), Life Technologies, Eugene, OR; anti-rabbit Alexa Fluor® 647 – LT A11031 (1:800), Life Technologies, Eugene, OR. Nuclei staining was obtained with Hoechst 33342 (1 μ g/mL; Thermo Fisher Scientific, Waltham, MA). The Wheat Germ Agglutinin (WGA) Alexa Fluor® 633 conjugate (W21404, 1:50, Thermo Fisher Scientific, Waltham, MA) was used to perform the volume measurement of hiPSC-CMs. Images were obtained by confocal microscopy using a Zeiss LSM 800 confocal microscope with a 40x-oil immersion objective.

Morphological analysis of 2D-cultured hiPSC-CMs

Analysis of ACTN2 protein aggregates was performed using ImageJ. Therefore, immunofluorescence images were imported to ImageJ and subjected to the “find Maxima” tool adjusting the signal threshold to 254 and 1 in fixed hiPSC-CMs and live-cell imaging experiments, respectively. The automatically generated image was then analyzed with the “find particles” tool, and areas of ACTN2 aggregates were automatically determined by ImageJ. Finally, ACTN2 areas were normalized to a control line or condition to express differences in areas as fold changes.

The volume measurement of hiPSC-CMs was performed using Imaris 7.6.1. software. Z-stack images were imported to Imaris and a surface was added. After choosing default parameters, the relevant channel (WGA) was selected. Next, a smooth surface was selected (surface area detail level of 0.312 μ m), and the threshold was set with the absolute intensity. Subsequently, the volume (μ m³) of the generated surface was calculated.

Live cell imaging of 2D-cultured hiPSC-CMs

After cardiac differentiation, hiPSC-CMs were transduced for 1 h in suspension at 37 °C with an adeno-associated virus serotype 6 (AAV6) carrying either the wild-type (WT; ACTN2-WT-HaloTag®) or the mutant (MUT; ACTN2-MUT-HaloTag®) construct under the control of the human *TNNT2* promoter at a MOI of 10,000 [4]. Ultimately, transduced hiPSC-CMs were seeded in Geltrex-coated (1:100; Gibco, Grand Island, NY) 96-well plates at a density of 2,500 - 5,000 cells per well. Live-cell imaging experiments were performed after 7 days in culture by adding TMR-ligand to the medium (0.1 mM; G8251, Promega, Madison, WI) for 30 min, specifically staining ACTN2-HaloTag® protein, followed by washing twice with culture medium and 10 min of Hoechst 33342 incubation (1 μ g/mL; H3570, Thermo Fisher Scientific, Waltham, MA), which was diluted in culture medium, followed by a final washing step. Images of hiPSC-CMs were acquired by confocal microscopy using a Zeiss LSM 800 confocal microscope, whereby only beating hiPSC-CMs were included to ensure cell viability.

Quantification of integration events was carried out in a blinded fashion and expressed as percentage of transduced hiPSC-CMs.

High-content imaging of 2D cultured hiPSC-CMs

HiPSC-CMs were either gently thawed or dissociated at day 17 into single cells using collagenase II [2] and transduced with an AAV6-*TNNT2*-mTagRFP-mWasabi-hLC3 (human LC3) tandem construct (MOI 10,000) for 1 h at 37 °C, while inverting the tube every 10 min, including a non-transduced control. HiPSC-CMs were seeded at a density of 2,500 cells in 96-well plates. After 30 days of culture, hiPSC-CMs were washed twice with PBS and fixed with Roti-Histofix (Roth, Karlsruhe, Germany) for 20 min at 4 °C. After three additional washing steps with PBS, hiPSC-CMs were stained with a *TNNT2* antibody (1:500; ab45932) and with Hoechst 33342 (1 µg/mL; Thermo Fisher Scientific, Waltham, MA), as previously described.[1,5] Automated image acquisition was performed in the Operetta high-content imaging system (Perkin Elmer), by capturing mWasabi signal (green), mTagRFP signal (red) and counterstained nuclei (Hoechst) and *TNNT2* (far-red), at 20x magnification. Since mWasabi is quenched in the acidic autolysosomes, green puncta were considered as autophagosomes. Assuming the red puncta to represent autophagosomes plus lysosomes, we then quantified the red puncta minus green puncta as autolysosomes in hiPSC-CMs. This was done by Harmony high-content imaging analysis software, by repurposing previously developed algorithms for determination of cardiomyocyte-relevant markers [6]. In brief, hiPSC-CMs were identified by displaying positive *TNNT2* signal and quantification of green and red puncta (number and intensity) was done in the whole cell area using Harmony in-built functions.

RNA isolation and gene expression analysis

Total RNA was extracted from 2D-cultured hiPSC-CMs using TRIzol® Reagent (Life Technologies) following the manufacturer's protocol. For expression analysis with the nanoString nCounter® Elements technology a total amount of 50 ng RNA was hybridized with a customized nanoString Gene Expression CodeSet (Table S4 in the Data Supplement) and analyzed using the nCounter® Sprint Profiler (nanoString). The mRNA levels were determined with the nSolver™ Data Analysis Software including background subtraction using negative controls and normalization to housekeeping genes (*ABCF1*, *CLTC*, *GAPDH*, *TUBB*; Table S4 in the Data Supplement) and expressed as fold change over *ACTN2*wt for the respective groups. For RNA sequencing analysis, samples derived from 2-3 independent differentiations were analyzed for each comparison. Therefore, total RNA was extracted from individual 2D cell pellet or EHT (2-3 biological replicates per differentiation) and after concentration measurement, equal amounts of RNA from 2-3 hiPSC-CMs in 2D-cultured or EHT format of each biological replicate (differentiation) were pooled and prepared as previously reported [1].

For RNA-seq analysis, gene abundance were quantified using salmon (v0.12.0) [7], and human gene annotations from gencode (version 33) for GRCh38 genome assembly were imported using R package tximport [8]. Counts normalization and differential gene expression analysis was performed using DESeq2 package [9]. Null variance of Wald test statistic output by DESeq2 was re-estimated using R package fdrtool [10] to calculate *P*-values (and adjusted using Benjamini-Hochburg method) for the final list of differentially expressed genes. FDR (BH-adjusted *P*-value) < 0.1 and log2 fold change < X was used as criteria for the final DE gene list.

Western blot analysis

Protein extraction from 2D-cultured hiPSC-CMs was based on a recent publication [11] with adjusted volumes as follow. For protein extraction from untreated 2D-cultured hiPSC-CMs, 50 μ L water with protease inhibitor cocktail was added to the cell pellet (about 440,000 cells/well) to obtain the cytosolic fraction. Subsequently, the membrane-enriched fraction was collected by adding 75 μ L SDS-buffer to the pellet. For protein extraction from treated 2D-cultured hiPSC-CMs, 100 μ L SDS-buffer was added to the cell pellet, the samples homogenized and spun down for 15 min at 14 000 rpm at RT. The supernatant was kept as total crude protein lysate. Western blot analysis was performed according to previous publications [12,13] with slight adaptations. For analysis of 30-day-old, 2D-cultured hiPSC-CMs, total crude protein lysates were evaluated by mixing 7.5 μ g of protein with 6x Laemmli buffer and subsequent separations on 4–15% Mini-PROTEAN Precast Gels (Bio-Rad, Hercules, CA) or 10%/12% self-casted acrylamide/bisacrylamide (29:1) gels. After electrophoresis, proteins were transferred to nitrocellulose or PVDF membranes and stained with the following antibodies: ACTN2 – A7811(1:10,000), Sigma-Aldrich, St. Louis, MO; TNNT2 – ab8295 (1:5000), Abcam, Cambridge, UK; GAPDH – 5G4 (1:5000), HyTest, Turku, Finland; LC3B – 2775 (1:1000), Cell Signaling Technology, Danvers, MA; SQSTM1 – P0067 (1:2000), Sigma-Aldrich, St. Louis, MO; ubiquitin – FK2 clone, BML-PW8810 (1:10,000), Enzo Life Sciences, Farmingdale, NY. Signals were detected using the SuperSignal West Dura Extended Duration Substrate (Thermo Fisher Scientific, Rockford, IL), acquired with the ChemiDoc Touch Imaging System (Bio-Rad, Hercules, CA) and quantified with the Image Lab software (Bio-Rad, Hercules, CA).

Measurement of chymotrypsin-like activity of the proteasome

Cell pellet (about 440,000 cells/well) of 2D-cultured hiPSC-CMs was dissolved in 50 μ L water with protease inhibitor cocktail (complete miniTM, Roche Diagnostics, Rotkreuz, Switzerland). After three freeze-thaw-cycles the cell lysate was homogenized by pipetting up and down and centrifuged at 4 °C, full speed for 30 min in a table-top centrifuge. The supernatant was kept as the cytosolic fraction. The measurement of the chymotrypsin-like activity of the proteasome was based on previous publications [11,14] and was slightly adapted for the evaluation in the cytosolic fraction of untreated 30-day-old, 2D-cultured hiPSC-CMs. To determine the activity of the 20S proteasome, 10 μ g of protein were used for the measurement which was performed in the absence of ATP and with a final concentration of 60 μ M of the synthetic fluorogenic substrate Suc-LLVY-AMC (Enzo Life Sciences, BML-P802).

Proteome analysis

Generation of protein samples: Samples derived from 3 independent differentiations were analyzed for each comparison. Initially, protein was extracted from individual 2D cell pellet or EHT (2-3 biological replicates per differentiation) by five cycles of freezing (liquid nitrogen) and thawing (30 °C, 1,400 rpm) in 8 M urea/2 M thiourea. Cell debris and insoluble material was separated by centrifugation (20,000 \times g, 1 h at 4 °C). After determination of protein content with a Bradford assay (Biorad, Munich, Germany), equal protein amounts from 2-3 hiPSC-CMs in 2D culture or EHT format of each biological replicate (differentiation) were pooled and subjected to proteolytic digestion.

Sample preparation: 4 μ g of total protein from each sample were reduced (2.5 mM DTT ultrapure, Invitrogen, for 15 min at 37 °C) and alkylated (10 mM iodoacetamide,

Sigma Aldrich, for 30 min at 37 °C). Proteolysis was performed using LysC (1:100 for 3 h at 37 °C), followed by tryptic digestion overnight at 37 °C (both from Promega, Madison, WI, USA). The tryptic digestion was stopped by adding acetic acid (final concentration 1%) followed by desalting using ZipTip- μ C18 tips (Merck Millipore, Darmstadt, Germany). Eluted peptides were concentrated by evaporation under vacuum and subsequently resolved in 0.1% acetic acid, 2% acetonitrile (ACN) containing HRM/iRT peptides (Biognosys, Zurich, Switzerland) according to manufacturer's recommendation.

Mass Spectrometry Measurements: Mass spectrometric (MS) data was recorded on a QExactive HFX mass spectrometer (Thermo Electron, Bremen, Germany). Before MS data acquisition tryptic peptides were separated by reverse phase chromatography (Accucore™ 150-C18, 25 cm x 75 μ m, 2.6 μ m C18, 150 Å) using an Ultimate 3000 nano-LC system (Thermo Scientific, Waltham, MA, USA) at a constant temperature of 40 °C and a flow rate of 300 nL/min.

To design a spectral library, MS/MS peptides were separated by 2 or 3 h-linear gradients with increasing acetonitrile concentration from 5 to 25% in 0.1% acetic acid, and data were recorded in data dependent mode (DDA). The MS scans were carried out in a m/z range of 350 to 1650 m/z . Data were acquired with a resolution of 60,000 and an AGC target of 3×10^6 at maximal injection times of 45 ms. The top 12 most abundant isotope patterns with charge ≥ 2 from the survey scan were selected for fragmentation by high energy collisional dissociation (HCD) with a maximal injection time of 22 ms, an isolation window of 1.3 m/z , and a normalized collision energy of 27.5 eV. Dynamic exclusion was set to 45 s. The MS/MS scans had a resolution of 15,000 and an AGC target of 1×10^5 .

The acquisition of MS data for relative quantitation was performed in data independent mode (DIA) after peptide pre-fractionation using a 120 min-linear gradient from 5% to 25% acetonitrile in 0.1% acetic acid. Briefly, the data was acquired in the m/z range from 350 to 1200 m/z , the resolution for MS was 120,000 and for MS/MS 30,000. The AGC target was 3×10^6 for MS and MS/MS. The number of DIA isolation windows was 70 of 11 m/z with 1 m/z overlap. For further details to the instrumental setup and the parameters for LC-MS/MS analysis in DDA and DIA mode see Table S5 and Table S6 in the Data Supplement.

Data analysis: Proteins were identified using Spectronaut™ Pulsar 13.4 software (Biognosys AG) against a spectral library generated from data-dependent acquisition measurements of individual and pooled samples of the study. The spectral library construction by Spectronaut was based on a database search using a human protein database (Uniprot vs 03_2019, 20404 entries) extended by sequences of bovine fibrinogen subunits A, B, and C. Because of the use of horse serum as medium supplement, sequences of 10 proteins reproducibly identified by proteotypic peptides were added to the database. The target-decoy search was performed with a parent mass error of ± 20 ppm, fragment mass error of 0.01 Da, and allowing full-tryptic peptides (trypsin/P cleavage rule) with a minimal peptide length of 6 amino acids and up to two internal cleavage sites. The search included carbamidomethylation at cysteine as fixed modification and oxidation at methionine and acetylation at protein N-termini as variable modifications. The generation of the ion library in Spectronaut™ v13.4.190802.43655 resulted in a constructed library consisting of 335,310 fragments, 30,756 peptides and 3,376 protein groups.

The Spectronaut DIA-MS analysis was carried out as described previously[15] with project specific modifications. Briefly, the following parameter settings were applied: dynamic MS1 and MS2 mass tolerance, dynamic XIC RT extraction window, automatic calibration, dynamic decoy strategy (library size factor = 0.1, minimum limit = 5000), protein Q-value cutoff of 0.01, precursor Q-value cutoff of 0.001. The search included variable and static modifications as described above for spectral library construction. A local cross run normalization was performed using complete profiles with a Q-value < 0.001. The MS2 peak area was quantified and reported. Missing values were parsed using an iRT profiling strategy with carry-over of exact peak boundaries (minimum Q-value row selection = 0.001). Only non-identified precursors were parsed with a Q-value > 0.0001. Ion values were parsed when at least 20% of the samples contained high quality measured values. Peptides were assigned to protein groups and protein inference was resolved by the automatic workflow implemented in Spectronaut. Only proteins with at least two identified peptides were considered for further analyses.

Data has been median normalized on ion level before statistical analysis was carried out on peptide level after exclusion of peptides with oxidized methionine using the algorithm ROPECA.[16] Binary differences have been identified by application of a moderate t-test.[17] Multiple test correction was performed according to Benjamini and Hochberg.[18] Variance within the data set was visualized by principal component analyses and differences in the protein pattern by Volcano plots.

Production and purification of adeno-associated virus vector particle

To generate the AAV transfer plasmid pFBGR-TNNT2-GFP, a PCR was performed (primer pair: 5'-GAG CGG CCG CAC GCG TCT CAG TCC ATT AGG AGC CAG TAG C-3' and 5'-GGG CGA ATT GGG TAC CTT ACT TGT ACA GCT CGT CCA TGC CG-3') and inserted into linearized pFBGR-GFP using the In-Fusion HD Cloning Kit (639648, Takara Bio Europe SAS, Kusatsu, Japan) according to the manufacturer's instructions.

The basis of the here applied mTagRFP-mWasabi-hLC3 tandem construct was kindly provided by Dr Zhou [19], and we modified and subcloned it in our lab.⁵⁶ Therefore, the vector pBudCE4.1-CMV (Invitrogen, Carlsbad, CA) was digested with *Bam*HI and *Hind*III. Touchdown PCR was performed using AmpliTaqGold (Thermo Fisher Scientific, Vilnius, Lithuania) and plasmid pcDNA3.1-mTagRFP-mWasabi-hLC3 as template with the following primer pair: 5'-TTC GAC AAG CTT ACC ATG AGC GAG CTG ATT AAG GAG AAC ATG CAC ATG A-3' and 5'-TTC GAC GGA TCC TTA CAC TGA CAA TTT CAT CCC GAA CGT CTC CTG GGA GG-3'. Ligation of the PCR product and the digested vector pBudCE4.1-CMV was performed using T4 Ligase according to manufacturer's instructions (Thermo Fisher Scientific, Vilnius, Lithuania). Subsequently, heat transformation using competent *E. coli* bacteria was performed. In short, bacteria were thawed on ice, 50 ng of DNA (ligation approach) was added, the tube once flicked and incubated for 30 min on ice. The heat shock was performed at 42 °C for 45 sec, followed by a 5-min incubation on ice. After the addition of 200 µL S.O.C. medium, the approach was incubated for 1 h at 37 °C gently shaking, before being plated on ampicillin agar plates. DNA of selected clones was isolated according to manufacturer's instructions (NucleoSpin Plasmid Mini kit, Macherey-Nagel, Düren, Germany) and evaluated by restriction digest and sequencing.

To express the mTagRFP-mWasabi-hLC3 tandem construct under control of the *TNNT2* promoter with an ampicillin resistance and the β -Globin IgG intron for higher transcription efficiency, the pGG2-*TNNT2*-insert plasmid was digested with

Bam HI and Nhe I . Touchdown PCR was performed using AmpliTaqGold and plasmid pBudCE4.1-CMV-mTagRFP-mWasabi-hLC3 as template with the primer pair: 5'-TTC GAC GGA TCC TTA CAC TGA CAA TTT CAT CCC GAA CGT CTC CTG GGA GG-3' and 5'-TTC GAC GCT AGC GCC ACC ATG AGC GAG CTG ATT AAG G-3'. Ligation of the PCR product and the digested pGG2-*TNNT2*-insert plasmid, heat transformation using competent *E. coli* bacteria and evaluation of selected clones by restriction digest and sequencing was performed as described above. For virus production, the pGG2-*TNNT2*-mTagRFP-mWasabi-hLC3 was inserted into pFBGR-*TNNT2* by In-Fusion cloning according to manufacturer's instructions. mTagRFP-mWasabi-hLC3 was amplified from pGG2-*TNNT2*-mTagRFP-mWasabi-hLC3 using PrimeStar GXL Polymerase (Takara Bio Europe SAS, Kusatsu, Japan) using 5'-AAC ATC GAT TGA ATT CAC CAT GAG CGA GCT GAT TAA GG-3' and 5'-TAT AGG GCG AAT TGG GTA CCT TAC ACT GAC AAT TTC ATC CCG A-3'. pFBGR-Ultra-*TNNT2*-GFP was cut with *EcoRI* and *KpnI* and both fragments were inserted simultaneously generating the AAV transfer plasmid pFBGR-Ultra-*TNNT2*-mTagRFP-mWasabi-hLC3.

For live-cell imaging experiments, WT- or MUT-*ACTN2* and HaloTag were assembled and inserted into pFBGR under control of a *TNNT2* promoter by In-Fusion cloning. Two fragments were generated by PCR using PrimeStar GXL Polymerase (Takara Bio Europe SAS, Kusatsu, Japan): *ACTN2* was amplified from plasmids either containing the WT or Mut sequence (c.740C>T; p.Thr247Met) that were kindly provided by Mathias Gautel using 5'-AAC ATC GAT TGA ATT CAC CAT GAA CCA GAT AGA GCC CGG-3' and 5'-GCT CGA GGA CAG ATCG CTC TCC CCG TAG AG-3'. HaloTag was amplified from the vector pFC14K-HaloTag®-CMV-Flexi® (G9651, Promega, Madison, WI) using 5'-GAT CTG TCC TCG AGC GAG GAT CTG TAC TTT CAG AGC GAT AAC G-3' and 5'-GGG CGA ATT GGG TAC CTT AAC CGG AAA TCT CCA GAG TAG ACA GC-3'. pFBGR-Ultra-*TNNT2*-GFP was digested with *EcoRI* and *KpnI* and both fragments were inserted simultaneously generating the AAV transfer plasmid pFBGR-Ultra-*TNNT2*-*ACTN2*-WT-/MUT-HaloTag. Final AAV transfer plasmids were confirmed by restriction digestion and sequencing. Recombinant baculovirus DNA carrying AAV genomic components was verified by PCR using *TNNT2/T7* promoter specific primers.

AAV were produced according to the "titerless infected-cells preservation and scale-up (TIPS)" also known as baculovirus-infected insect cells (BIIC).[20] Sf9 cells were transfected with recombinant baculovirus DNA derived from pFBGR-Ultra-*TNNT2*-mTagRFP-mWasabi-hLC3 or pFBGR-Ultra-*TNNT2*-*ACTN2*-WT-/MUT-HaloTag and pSR646-Ultra mCherry using TransIT®-Insect Transfection Reagent (MoBITec, Goettingen, Germany) according to the manufacturer's instructions. After 3 days, Sf9 cells (Novagen, Darmstadt, Germany) were collected, and 2E+07 fresh Sf9 cells were infected with this primary stock. On the next day, vital fluorescing TriEx Sf9 Cells (Novagen, Darmstadt, Germany) were collected and frozen at 2E+06 cells BIIC stocks in InsectXpress medium (Biozym Scientific GmbH, Verviers, Belgium)/10% DMSO. For AAV production, ~2E+08 fresh Sf9 cells were cultivated in InsectXpress Medium at a density of 2E+06 cells/ml. ~2E+06 Sf9 BIIC stocks containing the expression cassette *TNNT2*-mTagRFP-mWasabi-hLC3 or *TNNT2*-WT-/MUT-*ACTN2*-HaloTag and ~2E+06 Sf9 BIIC stocks containing the desired AAV packaging elements were added. AAV lysis buffer (50 mM Tris base, 100 mM NaCl, 5 mM MgCl₂, pH 8.5) was used for harvest. To remove cell debris, centrifugation for 20 min at 12,000 x g was performed, and vector containing lysates were purified using Iodixanol (OptiPrep, PROGEN Biotechnik, Heidelberg, Germany) step gradients. 40% Iodixanol layers

were harvested, and iodixanol was removed by ultrafiltration (Amicon Ultra-4, PLQK Ultracel-PL Membran, 50 kDa, MerckMillipore, Darmstadt, Germany).

Supplemental References

1. Prondzynski, M., Lemoine, M.D., Zech, A.T., Horvath, A., Di Mauro, V., Koivumaki, J.T., Kresin, N., Busch, J., Krause, T., Kramer, E., Schlossarek, S., Spohn, M., Friedrich, F.W., Munch, J., Laufer, S.D., Redwood, C., Volk, A.E., Hansen, A., Mearini, G., Catalucci, D., Meyer, C., Christ, T., Patten, M., Eschenhagen, T., Carrier, L. Disease modeling of a mutation in alpha-actinin 2 guides clinical therapy in hypertrophic cardiomyopathy. *EMBO Mol Med* **2019**,*11*, e11115.
2. Breckwoldt, K., Letuffe-Breniere, D., Mannhardt, I., Schulze, T., Ulmer, B., Werner, T., Benzin, A., Klampe, B., Reinsch, M.C., Laufer, S., Shibamiya, A., Prondzynski, M., Mearini, G., Schade, D., Fuchs, S., Neuber, C., Kramer, E., Saleem, U., Schulze, M.L., Rodriguez, M.L., Eschenhagen, T., Hansen, A. Differentiation of cardiomyocytes and generation of human engineered heart tissue. *Nat Protoc* **2017**,*12*, 1177-97.
3. Skryabin, B.V., Kummerfeld, D.M., Gubar, L., Seeger, B., Kaiser, H., Stegemann, A., Roth, J., Meuth, S.G., Pavenstadt, H., Sherwood, J., Pap, T., Wedlich-Soldner, R., Sunderkotter, C., Schwartz, Y.B., Brosius, J., Rozhdestvensky, T.S. Pervasive head-to-tail insertions of DNA templates mask desired CRISPR-Cas9-mediated genome editing events. *Sci Adv* **2020**,*6*, eaax2941.
4. Prondzynski, M., Kramer, E., Laufer, S.D., Shibamiya, A., Pless, O., Flenner, F., Muller, O.J., Munch, J., Redwood, C., Hansen, A., Patten, M., Eschenhagen, T., Mearini, G., Carrier, L. Evaluation of MYBPC3 trans-Splicing and Gene Replacement as Therapeutic Options in Human iPSC-Derived Cardiomyocytes. *Mol Ther Nucleic Acids* **2017**,*7*, 475-86.
5. Mosqueira, D., Mannhardt, I., Bhagwan, J.R., Lis-Slimak, K., Katili, P., Scott, E., Hassan, M., Prondzynski, M., Harmer, S.C., Tinker, A., Smith, J.G.W., Carrier, L., Williams, P.M., Gaffney, D., Eschenhagen, T., Hansen, A., Denning, C. CRISPR/Cas9 editing in human pluripotent stem cell-cardiomyocytes highlights arrhythmias, hypocontractility, and energy depletion as potential therapeutic targets for hypertrophic cardiomyopathy. *Eur Heart J* **2018**,*39*, 3879-92.
6. Mosqueira, D., Lis-Slimak, K., Denning, C. High-Throughput Phenotyping Toolkit for Characterizing Cellular Models of Hypertrophic Cardiomyopathy In Vitro. *Methods Protoc* **2019**,*2*.
7. Patro, R., Duggal, G., Love, M.I., Irizarry, R.A., Kingsford, C. Salmon provides fast and bias-aware quantification of transcript expression. *Nat Methods* **2017**,*14*, 417-9.
8. Sonesson, C., Love, M.I., Robinson, M.D. Differential analyses for RNA-seq: transcript-level estimates improve gene-level inferences. *F1000Res* **2015**,*4*, 1521.
9. Love, M.I., Huber, W., Anders, S. Moderated estimation of fold change and dispersion for RNA-seq data with DESeq2. *Genome Biol* **2014**,*15*, 550.
10. Strimmer, K. fdrtool: a versatile R package for estimating local and tail area-based false discovery rates. *Bioinformatics* **2008**,*24*, 1461-2.
11. Wenzel, K., Kramer, E., Geertz, B., Carrier, L., Felix, S.B., Konemann, S., Schlossarek, S. A Transgenic Mouse Model of Eccentric Left Ventricular Hypertrophy With Preserved Ejection Fraction Exhibits Alterations in the Autophagy-Lysosomal Pathway. *Front Physiol* **2021**,*12*, 614878.

12. Singh, S.R., Meyer-Jens, M., Alizoti, E., Bacon, W.C., Davis, G., Osinska, H., Gulick, J., Reischmann-Dusener, S., Orthey, E., McLendon, P.M., Molkentin, J.D., Schlossarek, S., Robbins, J., Carrier, L. A high-throughput screening identifies ZNF418 as a novel regulator of the ubiquitin-proteasome system and autophagy-lysosomal pathway. *Autophagy* **2021**, 1-16.
13. Vignier, N., Schlossarek, S., Fraysse, B., Mearini, G., Kramer, E., Pointu, H., Mougenot, N., Guiard, J., Reimer, R., Hohenberg, H., Schwartz, K., Vernet, M., Eschenhagen, T., Carrier, L. Nonsense-Mediated mRNA Decay and Ubiquitin-Proteasome System Regulate Cardiac Myosin-Binding Protein C Mutant Levels in Cardiomyopathic Mice. *Circ Res* **2009**, *105*, 239-48.
14. Schlossarek, S., Englmann, D.R., Sultan, K.R., Sauer, M., Eschenhagen, T., Carrier, L. Defective proteolytic systems in Mybpc3-targeted mice with cardiac hypertrophy. *Basic Res Cardiol* **2012**, *107*, 1-13.
15. Palma Medina, L.M., Becker, A.K., Michalik, S., Yedavally, H., Raineri, E.J.M., Hildebrandt, P., Gesell Salazar, M., Surmann, K., Pfortner, H., Mekonnen, S.A., Salvati, A., Kaderali, L., van Dijk, J.M., Volker, U. Metabolic Cross-talk Between Human Bronchial Epithelial Cells and Internalized Staphylococcus aureus as a Driver for Infection. *Mol Cell Proteomics* **2019**, *18*, 892-908.
16. Suomi, T., Elo, L.L. Enhanced differential expression statistics for data-independent acquisition proteomics. *Sci Rep* **2017**, *7*, 5869.
17. Phipson, B., Lee, S., Majewski, I.J., Alexander, W.S., Smyth, G.K. Robust Hyperparameter Estimation Protects against Hypervariable Genes and Improves Power to Detect Differential Expression. *Ann Appl Stat* **2016**, *10*, 946-63.
18. Benjamini, Y., Hochberg, Y. Controlling the False Discovery Rate: A Practical and Powerful Approach to Multiple Testing. *J R Statist Soc* **1995**, *57*, 289-300.
19. Zhou, C., Zhong, W., Zhou, J., Sheng, F., Fang, Z., Wei, Y., Chen, Y., Deng, X., Xia, B., Lin, J. Monitoring autophagic flux by an improved tandem fluorescent-tagged LC3 (mTagRFP-mWasabi-LC3) reveals that high-dose rapamycin impairs autophagic flux in cancer cells. *Autophagy* **2012**, *8*, 1215-26.
20. Wasilko, D.J., Lee, S.E., Stutzman-Engwall, K.J., Reitz, B.A., Emmons, T.L., Mathis, K.J., Bienkowski, M.J., Tomasselli, A.G., Fischer, H.D. The titerless infected-cells preservation and scale-up (TIPS) method for large-scale production of NO-sensitive human soluble guanylate cyclase (sGC) from insect cells infected with recombinant baculovirus. *Protein Expr Purif* **2009**, *65*, 122-32.